catalysts

MDPI

Review

Recent Advances in MXene-Based Cocatalysts for Photocatalytic Hydrogen Evolution

Yakun Song, Yifan Liao, Jiayi Meng, Quanmei Zhou, Yuchen Wei, Yuying Hu, Mohan Zhang, Hongyan Zhao and Weilin Dai *

State Key Laboratory of Porous Materials for Separation and Conversion, Shanghai Key Laboratory of Molecular Catalysis and Innovative Materials, Department of Chemistry, Fudan University, Shanghai 200438, China; 25110220088@m.fudan.edu.cn (Y.S.); 23110220051@m.fudan.edu.cn (Y.L.); 23110220061@m.fudan.edu.cn (J.M.); 24110220121@m.fudan.edu.cn (Q.Z.); 24110220083@m.fudan.edu.cn (Y.W.); 25110220036@m.fudan.edu.cn (Y.H.); 25110220140@m.fudan.edu.cn (M.Z.); 25210220018@m.fudan.edu.cn (H.Z.)
* Correspondence: wldai@fudan.edu.cn

Abstract

While MXenes are promising cocatalysts for photocatalytic hydrogen evolution, their roles are frequently oversimplified as merely conductive electron sinks. This review begins by revisiting the classical electron-sink mechanism of Ti_3C_2 and utilizes the CdSe/Ti_3C_2 and $Cd_{0.5}Zn_{0.5}S/Ti_3C_2$ systems to demonstrate how intimate interfaces, Fermi-level equilibration, Schottky junctions, and directional electron-transfer pathways synergistically couple charge separation with H* conversion. The discussion is then extended to multimetallic MXenes, using $ZnIn_2S_4/Mo_2TiC_2$ as a model, to highlight how metal-layer composition, local interfacial coordination, work-function differences, and hydrogen-adsorption energetics jointly regulate electron extraction and surface reaction kinetics. Special attention is given to surface terminations, which can reshape interfacial energetics and enable MXenes to transition between electron-sink and hole-mediated roles depending on the interface and working conditions. Furthermore, representative Nb_2C quantum-dot and VNbC solid-solution systems illustrate how nanoscale electric fields and multimetallic sites can expand MXene functionality beyond conventional electron extraction. Ultimately, this role-oriented framework advances the development of MXene cocatalysts from simple material integration toward controllable and programmable interfacial functions.

Keywords: MXenes; photocatalytic hydrogen evolution; electron sink; carrier-selective interfaces; multimetallic MXenes; surface terminations; working-state interfaces; role engineering

Check for updates

Academic Editor: Óscar Manuel González Díaz

Received: 27 August 2026
Revised: 16 September 2026
Accepted: 17 September 2026
Published: 22 September 2026

Copyright: © 2026 by the authors. Licensee MDPI, Basel, Switzerland. This article is an open access article distributed under the terms and conditions of the Creative Commons Attribution (CC BY) license.

1. Introduction

Photocatalytic H_2 production is not governed by light absorption alone; substantial energy is lost when photogenerated carriers recombine or fail to drive surface reactions. Since the photo-assisted electrolysis of water on TiO_2 reported by Fujishima and Honda [1], photocatalysis has developed toward particulate systems for solar-fuel production. Overall water splitting must be distinguished from sacrificial-agent-assisted H_2 evolution, which replaces water oxidation with donor oxidation and therefore evaluates only the reduction half-reaction [2]. Beyond the thermodynamic requirement of 237 kJ mol^{-1}, equivalent to 1.23 V, practical water splitting must overcome overpotentials and interfacial energy losses [3]. Most systems therefore remain below the efficiency required for practical im-

plementation [4], while durability, reactor cost, gas separation, safety, and system-level performance impose further constraints [5].

At the material level, these limitations arise mainly from two coupled bottlenecks: inefficient charge utilization and sluggish surface conversion. Photogenerated carriers may recombine in the bulk, at defects and grain boundaries, or at catalyst–solution interfaces before reaching reactive sites [6]. Productive separation therefore requires both a thermodynamic driving force and selective electron- and hole-transfer pathways [7]. Photoluminescence quenching, prolonged carrier lifetimes, or enhanced photocurrent alone cannot establish productive charge transfer because these signals may also reflect trapping or altered recombination [8]. Junction construction and facet engineering can direct carrier migration [9], while internal electric fields and polarization provide additional driving forces [10]. Spin regulation may further modify carrier dynamics and reaction pathways [11]. These strategies are effective only when the separated carriers retain sufficient redox power and are rapidly consumed through the multistep reactions involved in H_2 evolution and water oxidation [12]. Slow surface conversion instead causes charge accumulation and promotes recombination, directly coupling surface kinetics with carrier utilization [13].

Considerable progress has been achieved, but usually along only one part of this process. Facet-selective cocatalyst deposition on $SrTiO_3$:Al produced an external quantum efficiency approaching unity under ultraviolet irradiation [14], while particulate photocatalyst sheets achieved solar-to-hydrogen efficiencies above 1% [15]. Visible-light overall water splitting was extended using an oxysulfide photocatalyst [16] and a dye-sensitized Z-scheme system [17]. A 100 m^2 panel reactor further demonstrated large-scale solar hydrogen production, although its conversion efficiency remained limited [18]. These results highlight the persistent difficulty of combining efficient charge transport, rapid surface kinetics, broad light utilization, stability, and scalability. Cocatalysts address this gap by extracting carriers [19], lowering reaction barriers at surface sites [20], regulating interfacial energetics [21], and coordinating complementary reduction and oxidation processes [22]. For example, coordinatively unsaturated MoS_2 edges provide active sites for hydrogen evolution [23], but their effectiveness depends on intimate coupling with CdS to ensure efficient electron delivery [24]. In Pt-PdS/CdS, Pt accelerates proton reduction [25], whereas PdS promotes hole consumption, allowing the two interfaces to operate cooperatively [26]. Oxidation cocatalysts similarly suppress surface-hole accumulation on $BiVO_4$ [27,28], while spatially separated reduction and oxidation sites direct electrons and holes toward different half-reactions [29]. An effective cocatalyst must therefore connect directional carrier transfer with rapid and selective surface turnover rather than merely collect charge.

MXenes, generally described by the formula $M_{n+1}X_nT_x$, are two-dimensional transition-metal carbides, nitrides, or carbonitrides, where M denotes one or more transition metals; X represents C and/or N; T_x denotes surface termination species such as O, OH, F, or Cl; n determines the thickness of the M–X slab; and x represents the variable stoichiometric amount of surface terminations. Their two-dimensional morphology, accessible transition-metal surfaces, and adjustable electronic structures enable extensive semiconductor contact and short cross-interface transfer distances [30,31]. Their interfacial properties can also be tuned across multiple length scales and chemical environments [32,33]. The exfoliation of Ti_3AlC_2 established layered $Ti_3C_2T_x$ [34], and conductive $Ti_3C_2T_x$ films demonstrated the rapid transport potential of MXenes [35]. However, conductivity varies with flake quality, defect density, intercalated species, and oxidation [36], while changes in composition and surface functionalization can shift some MXenes away from metallic behavior [37]. Surface terminations introduce a further level of regulation. Lewis-acidic molten-salt reactions enable more controlled surface chemistry than conventional aqueous etching [38,39], and

covalent substitution has expanded MXene terminations beyond mixed -O, -OH, and -F to chalcogen, amino, halogen, and nearly termination-free surfaces [40]. These terminations alter surface dipoles and work functions [41], allowing MXenes to form electron- or hole-selective contacts depending on the coupled semiconductor [42]. Accordingly, Ti_3C_2 can accept electrons and promote H adsorption in metal-sulfide photocatalysts [43], whereas low-work-function $Ti_3C_2T_x$ may instead mediate hole transfer in appropriately aligned interfaces [44]. MXene function is therefore determined by its actual surface and interface rather than by nominal composition or conductivity alone.

Representative Nb_2C quantum-dot and VNbC solid-solution systems further illustrate how nanoscale electric fields and multimetallic sites can extend MXene functions beyond conventional electron extraction. Early MXene photocatalysts were mainly described as conductive electron sinks, yet this captures only one interface-dependent role. Existing reviews have comprehensively summarized MXene synthesis, photocatalytic applications, morphology, interfacial chemistry, and termination-dependent H_2 evolution [45,46].

Beyond these reviews, broader studies have examined MXenes in sustainable hydrogen production [47], photocatalytic CO_2 reduction [48], and diverse energy and environmental applications [49]. Early investigations demonstrated the potential of TiO_2/MXene composites [50] and CdS/Ti_3C_2 Schottky heterojunctions [51] for improving photocatalytic H_2 evolution. Studies on MXene/Bi_2WO_6 for CO_2 reduction [52] and TiO_2/Ti_3C_2 for dye degradation, in which Ti_3C_2 was proposed to act as a hole reservoir [53], further illustrate the reaction- and interface-dependent functions of MXenes. For photocatalytic H_2 evolution, sulfur-vacancy engineering in $ZnIn_2S_4$/$Ti_3C_2T_x$ [54] and surface-termination regulation in $ZnIn_2S_4$/$Ti_3C_2T_x$ [55] demonstrated the importance of defect chemistry and interfacial energetics in charge separation. Beyond conventional electron extraction, $Ti_3C_2T_x$/CdS heterostructures combined interfacial charge separation with photothermal enhancement [56], while CdS/MoS_2/Ti_3C_2 employed Ti_3C_2 and MoS_2 as hole- and electron-accepting components, respectively, to improve charge utilization and suppress photocorrosion [57]. Further studies of CdS/Ti_3C_2 Schottky heterojunctions provided experimental and theoretical evidence for interfacial charge transfer [58], whereas in situ construction of sandwich-like Ti_3C_2/rutile-TiO_2 interfaces strengthened interfacial contact and facilitated carrier transport [59]. Collectively, these findings highlight the importance of surface morphology, termination chemistry, and interface construction in determining MXene cocatalytic functions [60].

The present review takes a different perspective by focusing specifically on how MXene interfacial functions evolve in photocatalytic H_2 evolution. Rather than comparing material classes or cataloging reported activities, we organize the discussion around the relationships among interfacial electronic structure, metal-layer composition, surface terminations, dimensionality, charge-transfer direction, and catalytic-site function. Particular emphasis is placed on the experimental evidence required to assign these roles and on whether the proposed interface is retained under working conditions. In this review, MXenes are considered cocatalytic components when they primarily regulate carrier extraction, transport, interfacial energetics, or surface reaction kinetics without serving as the dominant light absorber. This role evolution is summarized in Scheme 1.

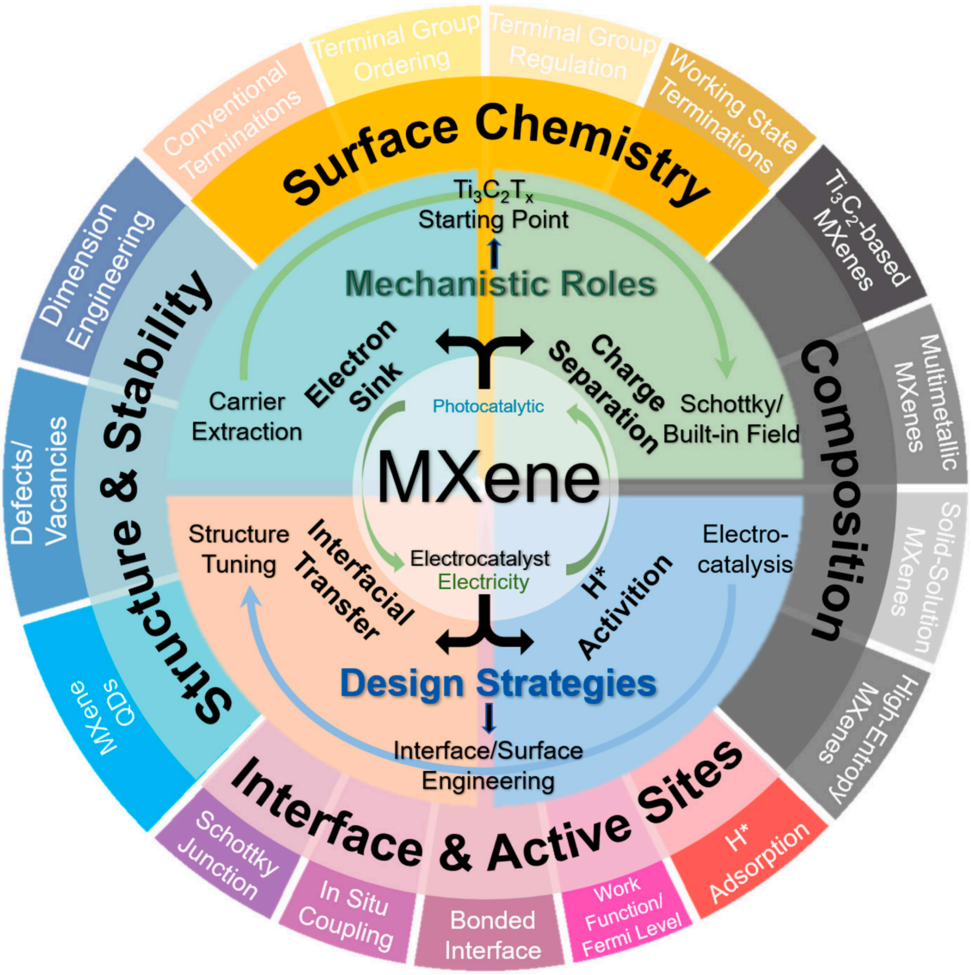

Scheme 1. Evolution of MXene cocatalytic roles in photocatalytic hydrogen evolution. The yellow and dark-blue arrows indicate the starting point of $Ti_3C_2T_x$ and interface/surface engineering, respectively. The green, light-blue, and orange curved arrows illustrate the conceptual links to composition, interface/active-site, and structure/stability engineering, respectively. The black arrows highlight charge-transfer and catalytic functions.

2. Classical Starting Point: $Ti_3C_2T_x$ as an Electron Sink

2.1. Electron Acceptance and Rapid Transport in $Ti_3C_2T_x$

$Ti_3C_2T_x$ is widely regarded as a conductive electron sink in photocatalytic H_2 evolution. Favorable energy-level alignment drives photogenerated electrons from the semiconductor to $Ti_3C_2T_x$, while its two-dimensional conductive framework supports rapid lateral transport. The extended interface also increases the contact area and shortens the cross-interface migration distance [60,61]. O-terminated Ti_3C_2 further provides favorable H adsorption energetics, establishing a direct link between electron transfer and proton reduction, as shown in Figure 1 [43].

Metal-sulfide systems provide representative evidence for this function. In $Zn_2In_2S_5$/$Ti_3C_2(O, OH)_x$, strong interfacial interaction promoted charge redistribution and carrier separation [62]. Growing ultrathin $ZnIn_2S_4$ nanosheets on both sides of $Ti_3C_2T_x$ created shorter and more continuous transfer pathways [63]. These results show that electron acceptance depends on both the electronic structure of $Ti_3C_2T_x$ and the quality of its contact with the semiconductor.

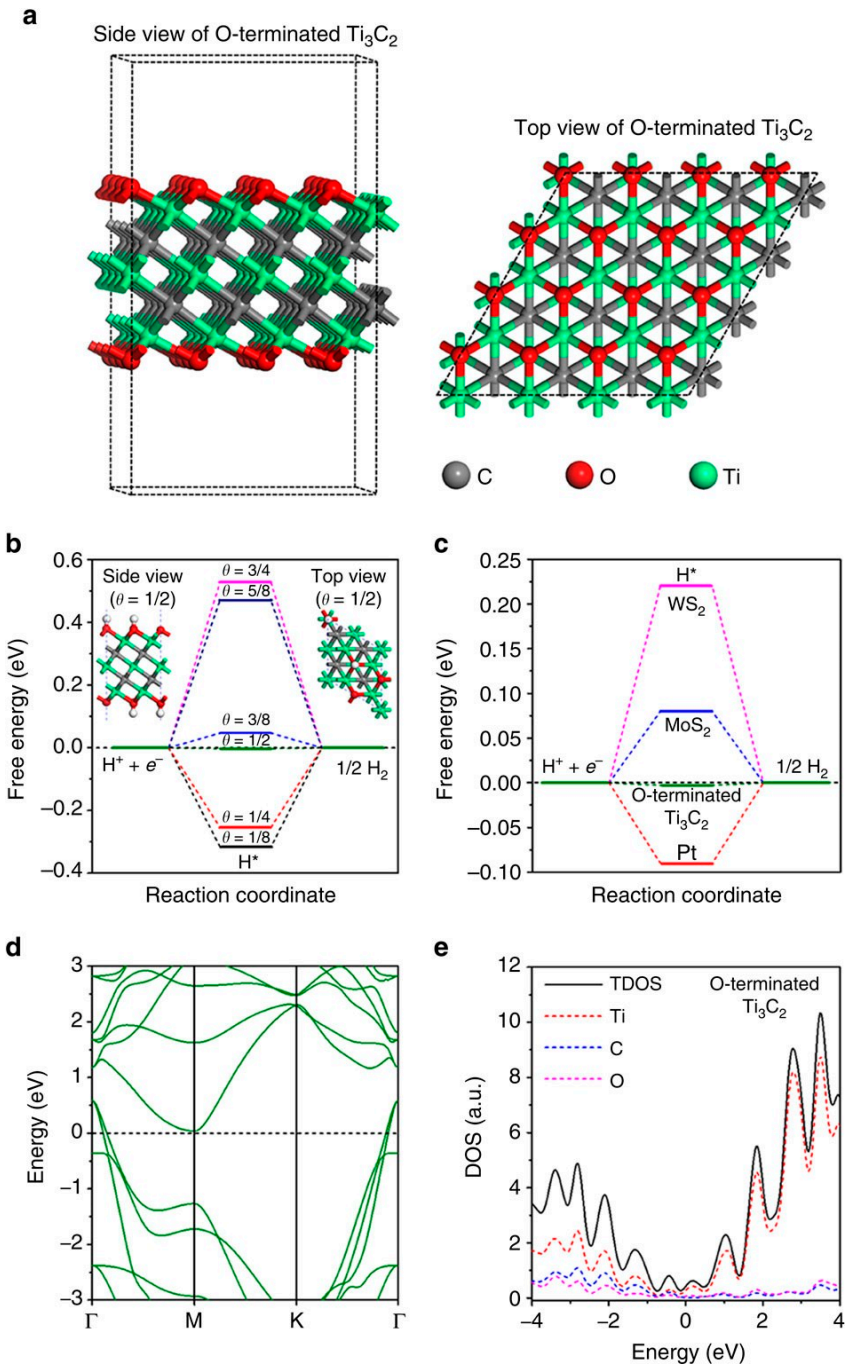

Figure 1. (**a**) Side and top views of the O-terminated Ti_3C_2 supercell. (**b**) Calculated free-energy diagrams for the hydrogen evolution reaction at different H* coverages. (**c**) Comparison of the hydrogen-adsorption free energies of O-terminated Ti_3C_2, Pt, MoS_2, and WS_2. (**d**) Calculated band structure. (**e**) Total and projected densities of states of O-terminated Ti_3C_2 [43]. Reproduced from Ref. [43] under CC BY 4.0.

Intimate coupling is therefore essential. Protonated g-C_3N_4/Ti_3C_2 Schottky heterojunctions reduced the resistance of interfacial electron transfer [64], while in situ grown Ti_3C_2@MIL-NH_2 composites strengthened contact through direct interface formation [65]. $Ti_3C_2T_x$ should thus be regarded as an interface-dependent electron acceptor rather than a universally effective conductive additive.

Electron extraction must also be followed by efficient delivery to reduction sites. In Ru/MXene/TiO_2, $Ti_3C_2T_x$ connected the photoactive semiconductor with Ru catalytic centers [66]. Oxidized g-C_3N_4/$Ti_3C_2T_x$ similarly combined electron collection with surface

sites favorable for H adsorption [67]. In these systems, $Ti_3C_2T_x$ acts as an electron relay that couples charge separation with surface H_2 evolution.

Morphology and surface chemistry further regulate this process. Face-to-face Ti_3C_2/g-C_3N_4 [68] and CdS/Ti_3C_2 [69] heterostructures increased the density of transfer interfaces. Plasma treatment promoted CdS nucleation and strengthened interfacial coupling [70], whereas $ZnIn_2S_4$ growth induced Ti_3C_2 delamination, exposed more surface area, and reduced restacking [71]. Rapid electron transport therefore requires suitable flake structure, continuous contact, favorable terminations, and efficient downstream electron consumption.

Overall, the electron-sink function of $Ti_3C_2T_x$ relies on four linked conditions: favorable energy alignment, intimate contact, continuous transport pathways, and rapid utilization of the transferred electrons. PL quenching, enhanced photocurrent, reduced impedance, and improved H_2 evolution indicate better carrier utilization, but they do not independently establish the transfer direction.

2.2. Interfacial Electron Migration from Semiconductors to $Ti_3C_2T_x$

Electron migration toward $Ti_3C_2T_x$ is governed by energy-level alignment and interfacial coupling. Fermi-level equilibration induces charge redistribution, band bending, and an interfacial electric field, driving photogenerated electrons from the semiconductor to $Ti_3C_2T_x$ while suppressing back-transfer. $Ti_3C_2T_x$ therefore acts as an electron-transfer intermediary that channels electrons toward reduction sites rather than as a terminal electron reservoir, as illustrated in Scheme 2 [72].

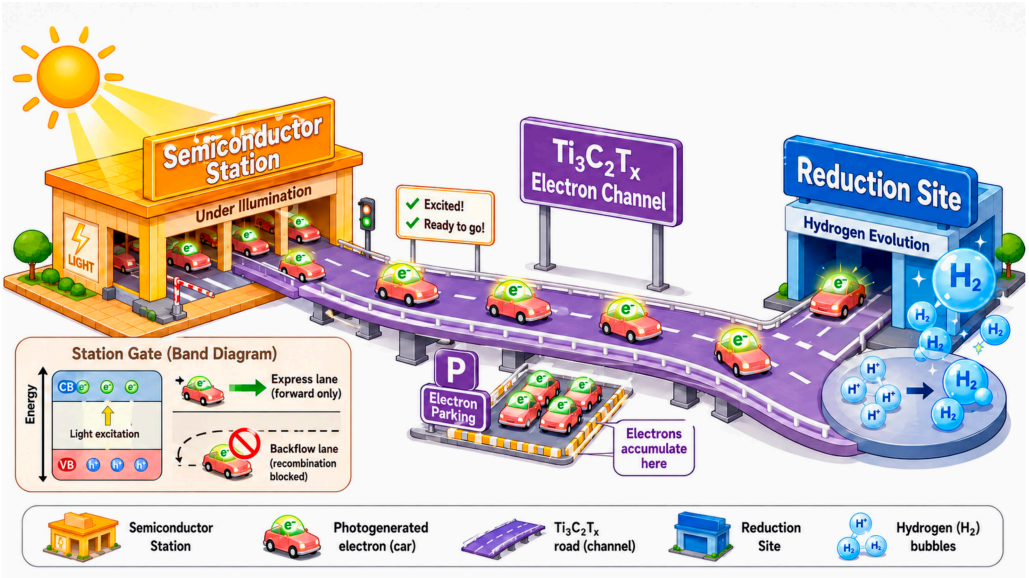

Scheme 2. Directional electron transfer from a semiconductor to $Ti_3C_2T_x$ and subsequent electron utilization for photocatalytic H_2 evolution.

The transfer rate depends strongly on interface geometry. In $Mn_{0.5}Cd_{0.5}S/Ti_3C_2$, nanoscale Schottky contacts accelerated electron extraction and reduced recombination [73]. Ligand-bridged CdS/$Ti_3C_2T_x$ further showed that molecular linkers can strengthen anchoring and improve electronic communication across the interface [74]. $InVO_4/Ti_3C_2$ [75] and Au/Ti_3C_2/g-C_3N_4 [76] extended this function from terminal electron acceptance to conductive relay behavior, in which Ti_3C_2 receives electrons from photoactive components and transports them toward catalytic sites.

Shortening the migration distance provides another route to faster transfer. Confining In_2S_3 within $Ti_3C_2T_x$ layers formed compact interfaces with reduced resistance [77], while

ultrathin $Cd_{0.8}Zn_{0.2}S$ nanosheets grown on Ti_3C_2 created similarly continuous transfer pathways [78]. A recent $Bi_2MoO_6/Ti_3C_2T_x$ heterostructure provides a direct structural example of such intimate semiconductor/MXene contact, with TEM and HRTEM resolving a well-defined heterointerface, as shown in Figure 2 [79]. What needs to be clarified here is in Figure 2d, the yellow and magenta boxes highlight Bi_2MoO_6 regions, whereas the red and cyan boxes indicate $Ti_3C_2T_x$ regions. The corresponding enlarged images in Figure 2e reveal characteristic lattice fringes with spacings of 0.325 and 0.202 nm for Bi_2MoO_6 and 0.31 and 0.26 nm for $Ti_3C_2T_x$, respectively. More complex Ru/Ti_3C_2-TiO_2/CdS [80] and $ZnIn_2S_4/Cd_{0.8}Zn_{0.2}S/Ti_3C_2$ [81] architectures further use Ti_3C_2 to connect semiconductor excitation with spatially separated reduction sites.

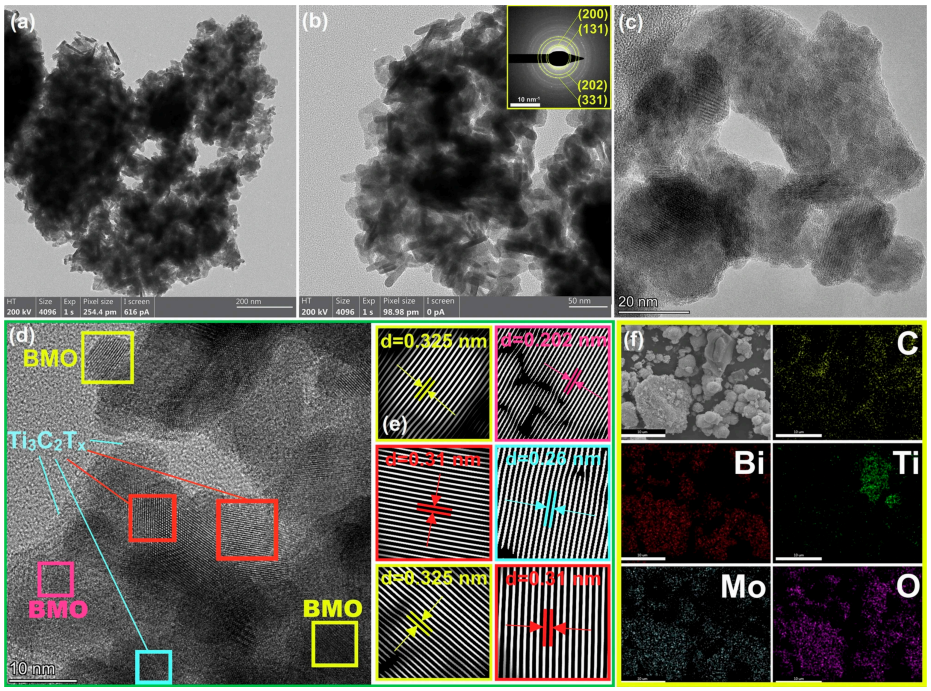

Figure 2. Interfacial microstructure of the $Bi_2MoO_6/Ti_3C_2T_x$ heterojunction: (**a**,**b**) TEM images; (**c**,**d**) HRTEM images resolving the closely contacted semiconductor/MXene interface; (**e**) inverse fast-Fourier-transform analysis of the interfacial region; and (**f**) EDS elemental mapping of the heterostructure [79]. Reproduced from Ref. [79] under CC BY 4.0.

Interfacial transport is also influenced by structural matching and dimensionality. Lattice-coherent Te/In_2O_3@MXene interfaces reduced structural discontinuity and transport barriers [82]. Electron migration is therefore controlled by the work-function difference, bonding configuration, interface continuity, dimensionality, and rate of electron consumption.

A convincing assignment of semiconductor-to-$Ti_3C_2T_x$ electron transfer requires convergent evidence. Work-function measurements, UPS, Kelvin-probe analysis, light-irradiated XPS, transient spectroscopy, and charge-density calculations can establish the energetic feasibility and transfer direction. By contrast, PL quenching, increased photocurrent, reduced impedance, or enhanced H_2 evolution demonstrate improved carrier utilization but cannot alone prove electron migration toward $Ti_3C_2T_x$.

These measurements address different levels of the mechanism: energetic measurements establish whether transfer is feasible, whereas time-resolved and spatially resolved probes determine whether it actually occurs and on what timescale.

2.3. Mechanistic Evidence from Representative CdSe- and $Cd_{0.5}Zn_{0.5}S$-Based Systems

Our group used CdSe/Ti_3C_2 and $Cd_{0.5}Zn_{0.5}S$/Ti_3C_2 as model systems to establish the electron-sink function of Ti_3C_2 through complementary structural, energetic, spectroscopic, kinetic, and theoretical evidence [83–85].

In CdSe/Ti_3C_2, CdSe nanorods were grown directly on Ti_3C_2 nanosheets to form an intimate 1D/2D interface [84]. UPS and work-function measurements indicated electron redistribution from CdSe to Ti_3C_2 after contact, leading to Fermi-level equilibration and interfacial band bending. XPS consistently showed electron depletion on CdSe and enrichment on Ti_3C_2. Under illumination, the Cd and Se peaks shifted toward higher binding energies, whereas the Ti peak shifted toward lower binding energy, supporting photoelectron migration from CdSe to Ti_3C_2. KPFM and selective Au photodeposition further located electron accumulation on the Ti_3C_2 component. The light-induced XPS response is shown in Figure 3 [84], where the arrows indicate binding-energy shifts of +0.4 eV for Cd 3d, +0.3 eV for Se 3d, and −0.2 eV for Ti 2p under illumination.

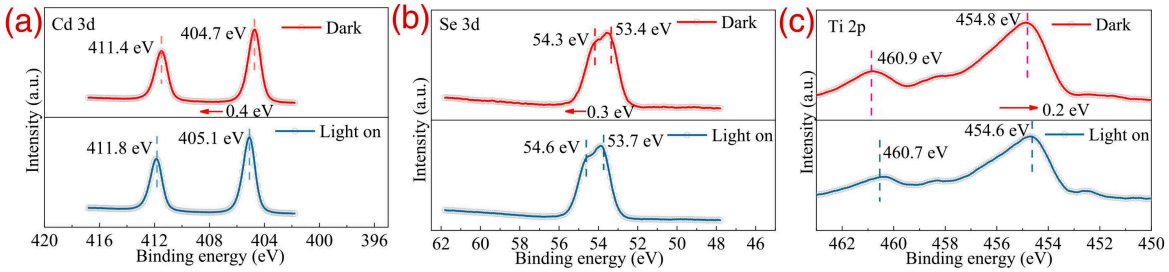

Figure 3. High-resolution in situ XPS spectra of (**a**) Cd 3d, (**b**) Se 3d, and (**c**) Ti 2p for the CdSe/Ti_3C_2 composite under dark and light-irradiation conditions [84].

This transfer also produced clear kinetic consequences. The composite exhibited stronger photocurrent, lower interfacial resistance, quenched photoluminescence, and a shorter fluorescence lifetime. DFT calculations revealed electron accumulation on Ti_3C_2 and an increased density of states near the Fermi level. Ti_3C_2 also improved H adsorption energetics, showing that the extracted electrons were coupled to surface H_2 evolution rather than merely stored at the interface [84].

The $Cd_{0.5}Zn_{0.5}S$/Ti_3C_2 system extended this mechanism to a single-layer MXene interface [85]. $Cd_{0.5}Zn_{0.5}S$ nanorods were uniformly anchored on Ti_3C_2 nanosheets, enabling efficient extraction at a Ti_3C_2 loading of only 0.5 wt%. Light-irradiated XPS showed electron depletion from $Cd_{0.5}Zn_{0.5}S$ and enrichment on Ti_3C_2. Femtosecond transient absorption further identified faster depopulation of the semiconductor excited state after coupling, directly linking the interface structure to ultrafast electron transfer. The corresponding charge-transfer response is shown in Figure 4 [85]. The arrows indicate binding-energy shifts of +0.4 eV for Cd 3d, +0.5 eV for Zn 2p, +0.4 eV for S 2p, and −0.2 eV for Ti 2p under illumination. The faint gray traces represent the experimental spectra, while the colored curves show the corresponding fitted profiles.

Together, these systems provide complementary energetic and ultrafast spectroscopic evidence for the electron-transfer pathway summarized in Scheme 2.

The CdSe/Ti_3C_2 system establishes the transfer direction through UPS, KPFM, illuminated XPS, photodeposition, and DFT, whereas $Cd_{0.5}Zn_{0.5}S$/Ti_3C_2 provides additional ultrafast spectroscopic evidence. Nevertheless, illuminated-XPS shifts should be interpreted together with energetic and kinetic measurements rather than used alone to quantify transferred electrons [86]. Schottky-barrier height and interfacial bonding can further alter the transfer process [87], while surface terminations and adsorbed species may change the working-state role of $Ti_3C_2T_x$ [88].

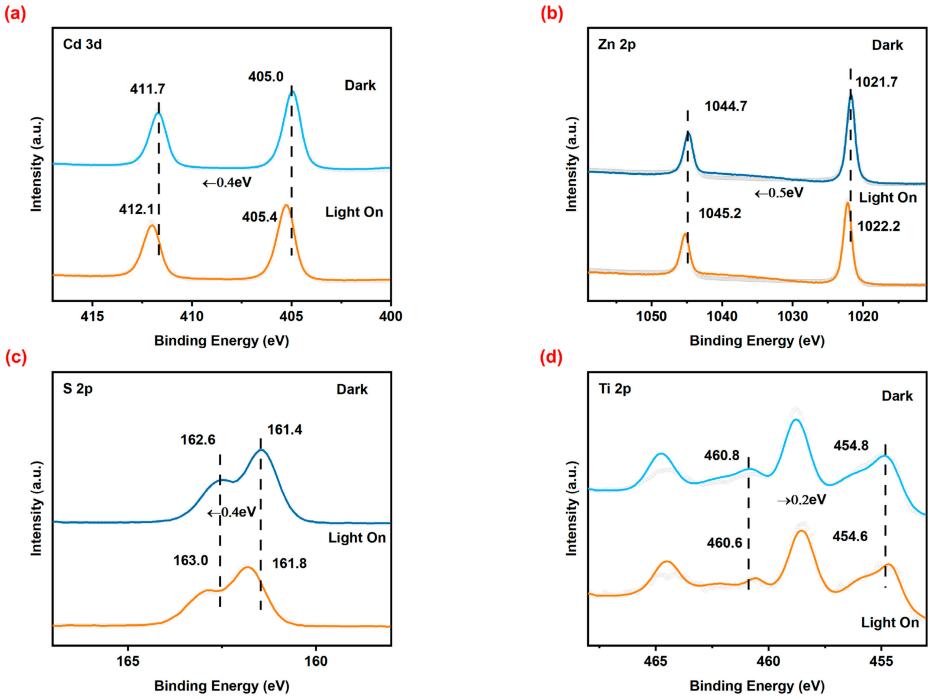

Figure 4. High-resolution in situ XPS spectra of Cd 3d (**a**), Zn 2p (**b**), S 2p (**c**), and Ti 2p (**d**) of $Cd_{0.5}Zn_{0.5}S$ and $Cd_{0.5}Zn_{0.5}S/Ti_3C_2$ [85].

2.4. From Physical Contact to Chemically Coupled Interfaces

MXene-based interfaces have evolved from weak physical contact toward confined, chemically bonded, and atomically coupled junctions. The electron-transfer function of $Ti_3C_2T_x$ depends not only on conductivity and work function, but also on interfacial continuity and coupling strength. Mechanical or ultrasonic mixing commonly produces discontinuous van der Waals contact and relatively high transfer resistance.

Electrostatic assembly improves dispersion and contact by exploiting the charged MXene surface. Protonated C_3N_5, for example, was assembled with negatively charged Ti_3C_2 nanosheets to form a closely contacted Schottky interface that promoted electron migration toward Ti_3C_2 [89]. Ligand bridging provides stronger anchoring and more continuous pathways across $CdS/Ti_3C_2T_x$ interfaces [74].

In situ growth further converts geometrical contact into direct electronic coupling. In $SrTiO_3/Ti_3C_2$, $Sr(OH)_2$ partially etched surface Ti atoms while inducing $SrTiO_3$ nucleation. The resulting chemical bonding and Ti vacancies promoted carrier separation more effectively than physical mixing [90]. This comparison shows that interface continuity and electronic interaction, rather than simple component coexistence, determine transfer efficiency.

Interfacial bonds can also function as direct charge-transfer channels. In sandwich-like $WO_3/Ti_3C_2/ZnIn_2S_4$, Ti-S and Ti-O-W bonds connected Ti_3C_2 with $ZnIn_2S_4$ and WO_3, respectively. These bonds enhanced orbital coupling, shortened transfer distances, and enabled directional charge migration, while the sandwich architecture suppressed MXene oxidation [91]. Bonded Ti_3C_2/carbon nitride interfaces similarly showed that chemical coupling can regulate both electronic interaction and Schottky-barrier formation [87].

More precise strategies have progressed toward lattice coherence and atomic-scale bridging. Lattice matching reduces structural discontinuity and carrier scattering [81]. In Ru-Cd_1-xS/$Ti_3C_2T_x$, vacancy-mediated Ru-O bonds bridged the heterointerface, strengthened the built-in electric field, and accelerated charge transfer to approximately 1.3 ps [92].

MXene interface engineering has therefore progressed from weak physical contact toward increasingly confined, chemically bonded, and atomically defined junctions. Interfacial coupling is thus a key structural variable, but its effect must be considered together with MXene composition, surface chemistry, and reaction kinetics.

2.5. Design Principles for Directional Electron Transfer

The studies above show that directional charge transfer at MXene interfaces is governed by three linked factors: energetic alignment, interfacial coupling, and carrier consumption. Work-function matching and Fermi-level equilibration determine band bending and the built-in electric field, defining whether an MXene acts as an electron acceptor, transport mediator, or hole-extraction component [93]. Its role should therefore be assigned from the actual interface rather than from conductivity alone.

Once the transfer direction is established, interfacial coupling controls the transfer rate. Schottky contacts, interfacial Ti-O-W or Ti-S bonds, lattice-coherent junctions, and vacancy-mediated bridges can reduce resistance and shorten migration distances [81,90–92]. Effective interfacial coupling should reduce charge-transfer resistance while preserving favorable band alignment and accessible catalytic sites; the optimal barrier height and bonding configuration are therefore system-specific rather than universally maximized. The transferred carriers must also reach accessible active sites, where vacancies or single atoms can couple charge separation with proton reduction [92,94].

These principles connect the classical $Ti_3C_2T_x$ electron-sink model with the broader role diversification discussed in the following section. Representative MXene-based photocatalysts and their reported H_2-evolution performances are summarized in Table 1, although differences in reaction conditions should be considered when comparing activities. Mechanistic assignment should therefore distinguish three levels of evidence. Work-function and band-alignment measurements establish the thermodynamic driving force, time-resolved spectroscopy resolves the transfer kinetics, and active-site or intermediate analyses determine whether the transferred carriers are productively consumed. Overall, energetic alignment determines transfer direction, interfacial coupling controls transfer kinetics, and local coordination governs carrier consumption.

The reported activities should not be interpreted as a direct ranking because catalyst loading, sacrificial reagents, irradiation conditions, wavelength ranges, reactor geometry, and gas-quantification methods vary across studies. Within-study comparisons with the parent semiconductor or benchmark cocatalyst are therefore generally more informative than absolute H_2-evolution rates across different reports. AQY/AQE, MXene loading, stability, and matched controls should be considered together with mass-normalized activity. Table 1 also illustrates that similar activity enhancements can arise from fundamentally different interfacial functions. Binary Schottky interfaces mainly promote electron extraction, whereas multicomponent architectures can provide parallel carrier-transfer pathways. For example, the 2D/2D/2D $ZnIn_2S_4$/g-C_3N_4/Ti_3C_2 heterostructure combines an S-scheme pathway between $ZnIn_2S_4$ and g-C_3N_4 with a Schottky-mediated electron-transfer channel from g-C_3N_4 to Ti_3C_2, reaching an H_2 evolution rate of 2.452 mmol g^{-1} h^{-1}. This example shows that Ti_3C_2 can function as one branch of a coordinated carrier-routing network rather than solely as a terminal electron sink.

Performance alone, however, does not establish the interfacial function of an MXene. Mechanistic assignment requires complementary evidence for energetic alignment, charge-transfer direction, carrier dynamics, and catalytic-site function. Table 2 therefore compares representative systems according to the key evidence supporting their proposed MXene interfacial roles.

Table 1. Representative performance and interfacial roles of MXene-based photocatalysts for H_2 evolution.

Photocatalyst	MXene Form/Interface Role	Construction Mode	Reported Test Conditions	H_2 Evolution Rate (mmol g^{-1} h^{-1})	AQY/AQE	Reported Benchmark or Stability	Ref.
UZNs–MNs–UZNs $ZnIn_2S_4/Ti_3C_2T_x$	$Ti_3C_2T_x$ nanosheets; sandwich-like 2D/2D Schottky interfaces	In situ hydrothermal growth	TEOA; 300 W Xe lamp	3.475	20.41% at 400 nm	6.6-fold higher than pristine $ZnIn_2S_4$; excellent stability reported	[63]
Protonated g-C_3N_4/Ti_3C_2	Ti_3C_2 nanosheets; electron-accepting Schottky contact	Protonation-assisted assembly	TEOA; 300 W Xe lamp	0.727	8.6% at 400 nm	Strong interfacial interaction reported; quantitative cycle retention not reported	[64]
CdS@MoS_2/Ti_3C_2	Ti_3C_2 electron-transfer layer plus MoS_2 HER cocatalyst	Microwave–hydrothermal construction	Lactic acid; 300 W Xe lamp	14.880	n.r.	Enhanced resistance to CdS photocorrosion and improved cycling behavior	[57]
$ZnIn_2S_4$/10% Mo_2TiC_2	Few-layer Mo_2TiC_2; tightly bound Schottky interface	In situ solvothermal growth	10 mg catalyst; simulated sunlight; sacrificial agent not reported in the original study	4.300	0.75% at 350 nm	3.8-fold higher than $ZnIn_2S_4$ and higher than $ZnIn_2S_4$/1% Pt	[95]
25% Mo_2TiC_2/ZnCdS	Mo_2TiC_2 nanosheets; strongly coupled 2D/0D Ohmic contact	Physical mixing	6 mg catalyst; 30 mL 10 vol% lactic acid; 5 W LED	17.730	16.22% at 475 nm	3.15-fold higher than ZnCdS	[96]
$CdIn_2S_4/Mo_2TiC_2$	Mo_2TiC_2 nanosheets; Schottky electron-accepting cocatalyst	Physical stirring and grinding	Detailed irradiation and sacrificial-agent conditions not reported in the original study	3.350	0.71% at 450 nm.	55.83-fold higher than $CdIn_2S_4$; activity maintained over four cycles	[97]
N-Ti_3C_2 MQDs/CdS	N-doped Ti_3C_2 quantum dots; 0D/1D charge-transfer junction	Self-assembly	Visible-light photocatalysis; detailed conditions not reported in the original study	17.094	n.r.	14.79-fold higher than pure CdS	[98]
5.5 wt% Ti_3C_2 QD/PGCN	Ti_3C_2 quantum dots; 0D/3D Schottky and photothermal interface	Electrostatic self-assembly	TEOA; 300 W Xe lamp	4.041	11.8% at 420 nm	15.24-fold higher than pristine CN and 3.53-fold higher than PGCN	[99]
$ZnIn_2S_4$/g-C_3N_4/Ti_3C_2	Ti_3C_2 nanosheets; Schottky electron-extraction branch integrated with a $ZnIn_2S_4$/g-C_3N_4 S-scheme	Hydrothermal	300 W Xe lamp (>420 nm); 10 mg catalyst; 80 mL H_2O/TEOA (72/8 mL); Pyrex reactor; GC detection.	2.452	13.1% at 365 nm	1.5-fold higher than $ZnIn_2S_4/Ti_3C_2$ (ZM-3) and 1.6-fold higher than g-$C_3N_4/ZnIn_2S_4$ (CZ-3)	[100]

Table 2. Critical experimental evidence required for assigning MXene interfacial functions in photocatalytic H_2 evolution.

Representative System	Interface/Assigned MXene Role	Proposed e−Transfer	Energetic Basis	Key Charge-Transfer Evidence	Active-Site Evidence	Photocatalytic Performance/Stability	Confidence	Ref.
$CdSe/Ti_3C_2$	1D/2D interface; electron acceptor/relay	$CdSe \rightarrow Ti_3C_2$	$\Phi(CdSe) = 4.73$ eV; $\Phi(Ti_3C_2) = 6.34$ eV; band bending	UPS; light–XPS; KPFM; Au photodeposition; DFT	DFT-supported favorable H* adsorption	0.763 mmol g^{-1} h^{-1}; AQE 1.3%; stable for 5 cycles; post-XRD/TEM	High	[84]
$Cd_{0.5}Zn_{0.5}S/Ti_3C_2$	1D/2D interface; electron acceptor	$CZS \rightarrow Ti_3C_2$	Fermi-level equilibration/Schottky alignment	Light–XPS; fs-TA; DFT	Improved H-related energetics by DFT	15.56 mmol g^{-1} h^{-1}; AQE 18.4% at 350 nm; stable for 5 cycles	High	[85]
$ZnIn_2S_4/Mo_2TiC_2$	Tightly coupled 2D/2D Schottky interface; electron extractor	$ZIS \rightarrow Mo_2TiC_2$	Work-function mismatch; Schottky barrier	In situ/light–XPS; DFT charge redistribution	HER-site/ΔG_{H^*} evidence incomplete	4.30 mmol g^{-1} h^{-1}; stability reported	Moderate	[95]
$ZnCdS/Mo_2TiC_2$	2D/0D Ohmic interface; electron-transfer mediator	$ZnCdS \rightarrow Mo_2TiC_2$	Ohmic-contact alignment	XPS; DFT; carrier-separation measurements	d-band/H-adsorption regulation	17.73 mmol g^{-1} h^{-1}; AQE 16.22% at 475 nm; lactic acid; stable	Moderate	[96]
$ZnIn_2S_4/g$-C_3N_4/Ti_3C_2	2D/2D/2D S-scheme/Schottky network; Ti_3C_2 electron-accepting branch	g-$C_3N_4 \rightarrow Ti_3C_2$; ZIS/g-C_3N_4 S-scheme	Band alignment supports dual pathways	XPS/spectroscopic evidence; direct ultrafast evidence n.r.	Direct MXene HER-site evidence n.r.	2.452 mmol g^{-1} h^{-1}; TEOA; cycling stability reported	Moderate	[100]

Table 2 highlights a hierarchy of mechanistic evidence. Energetic alignment establishes whether charge transfer is feasible, whereas light-induced XPS, KPFM, photodeposition, and time-resolved spectroscopy provide stronger evidence for its direction and kinetics. Active-site-sensitive measurements are further required to connect transferred carriers with H_2 evolution. Thus, PL quenching, enhanced photocurrent, reduced impedance, or increased activity alone cannot establish a specific MXene interfacial role.

Taken together, Tables 1 and 2 show that high photocatalytic activity and reliable mechanistic assignment are complementary but distinct criteria. Rational MXene interface design therefore requires not only favorable performance, but also a clear connection among energetic alignment, interfacial coupling, carrier-transfer kinetics, and catalytic-site function. These relationships provide the basis for understanding how metal-layer composition and surface chemistry can further diversify MXene interfacial roles, as discussed in the following section.

3. Role Diversification Through Metal-Layer and Surface-Termination Engineering

3.1. Multimetallic MXenes and Surface Terminations as Electronic-Structure Regulators

The electronic properties of MXenes are jointly determined by the carbide or nitride framework and the chemistry of the exposed surface. Hart et al. showed that deintercalation and partial removal of surface species converted the apparent semiconductor-like transport of $Mo_2TiC_2T_x$ and Ti_3CNT_x into metallic behavior [101]. Measured conductivity therefore reflects not only the intrinsic band structure, but also interflake transport, residual intercalants, and surface chemistry.

Surface terminations have consequently become controllable structural variables. Postsynthetic exchange has expanded the accessible surface chemistry beyond conventional O/OH/F terminations to N-, chalcogen-, and halogen-containing surfaces [40]. More broadly, recent screening across diverse MXene backbones and termination chemistries illustrates the large compositional space available for surface regulation, as summarized in Figure 5 [102], where the red highlights the 29 candidate M-site elements, including selected f-block elements, black denotes the X-site elements (C and N), and blue represents the 11 candidate surface-termination elements (T). The same color scheme is used in the structural models above the periodic table.

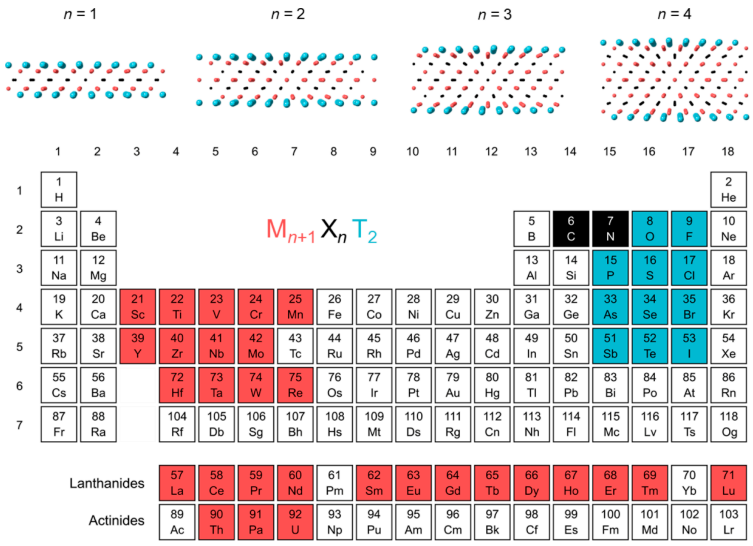

Figure 5. MXene compositional space explored across transition-metal species (M), carbon and nitrogen layers (X), surface terminations (T), and different layer thicknesses (n) [102]. Reproduced from Ref. [102] under CC BY 4.0.

Beyond expanding the accessible chemical space, increasing control over termination identity and uniformity can directly regulate charge transport. Uniformly halogen-terminated Ti_3C_2 exhibits strongly termination-dependent conductivity and carrier mobility, with reduced electronic scattering on chemically well-defined surfaces, as shown in Figure 6 [103]. In Figure 6d–f, the light-blue, gray, and purple spheres represent Ti, C, and Cl atoms, respectively, while the green and red spheres in the mixed-termination model indicate Cl and O atoms, respectively. These results show that termination identity and uniformity directly regulate electronic structure and carrier transport.

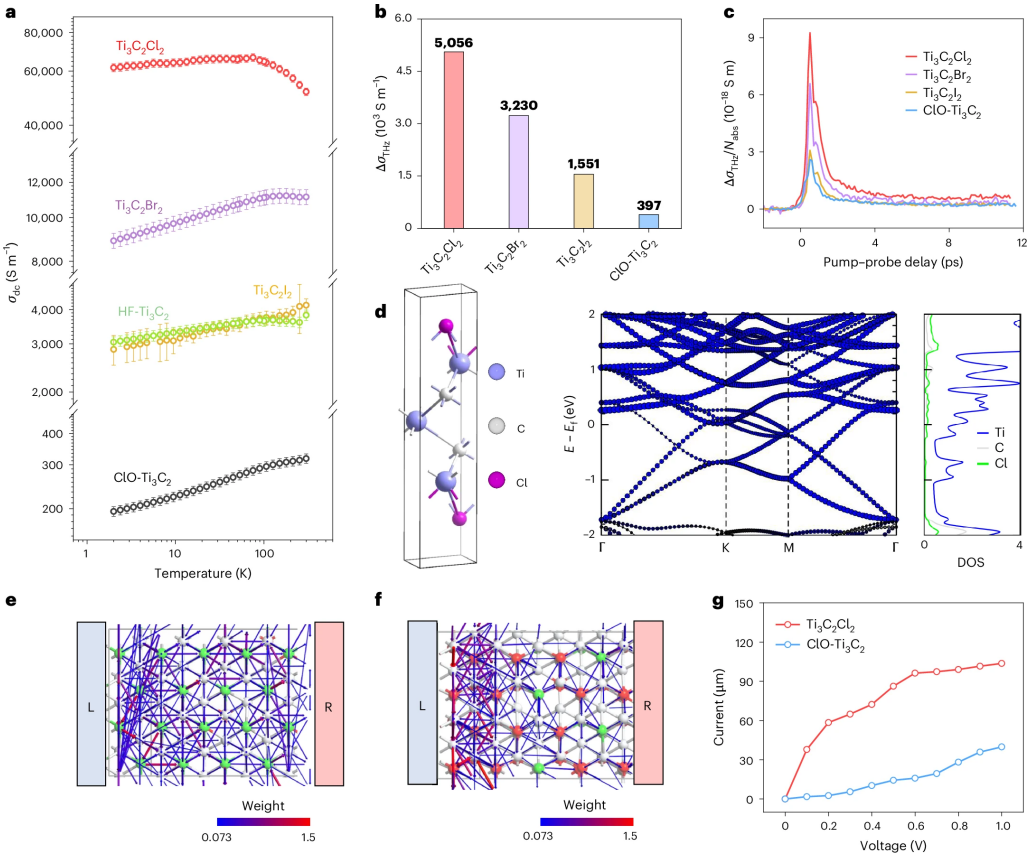

Figure 6. Charge-transport properties of uniformly halogen-terminated Ti_3C_2: (**a**) temperature-dependent direct-current conductivity; (**b**) terahertz conductivity; (**c**) time-resolved terahertz photoconductivity; (**d**) calculated structure, band structure, and density of states of $Ti_3C_2Cl_2$; (**e**,**f**) simulated electron transport and scattering in $Ti_3C_2Cl_2$ and ClO-Ti_3C_2; and (**g**) calculated current–voltage characteristics [103]. Reproduced from Ref. [103] under CC BY 4.0.

Multimetallic MXenes provide a complementary route for tuning the underlying electronic framework. In ordered $M'2M''C_2T_x$ and $M'2M''C_3T_x$, the outer M' layers interact directly with terminations and adsorbates, whereas the inner M'' layers regulate lattice stability and charge redistribution. Changing the M'/M'' combination reconstructs the metal d states near the Fermi level while generally retaining conductive pathways [104]. Experimental conversion of Mo_2TiAlC_2 into $Mo_2TiC_2T_x$ further showed that phase composition and surface chemistry affect catalytic charge transport through different mechanisms [105]. Nominal stoichiometry alone is therefore insufficient to define the functional electronic structure.

At the orbital level, coupling between outer-metal d orbitals and termination O p orbitals links metal-layer composition directly to surface electronic states [106]. Computational studies likewise reveal substantial variations in conductivity, orbital occupation, and catalytic properties among ordered carbide [107], carbonitride [108], and broader

multimetallic MXenes [109]. The metal layers define the d-electron framework, while the terminations determine how this framework is expressed at the interface.

These variables cannot be optimized independently. Synthesis and processing can simultaneously alter intercalants, termination distributions, defects, and structural disorder, so the measured electronic properties often reflect their combined effects rather than a single structural factor [110]. Synthetic strategies have therefore progressed from poorly defined O/OH/F surfaces toward more chemically controlled MXenes, including Lewis-acid-derived halogen terminations [38] and direct synthesis of uniformly terminated structures [111].

MXenes should thus be treated as coupled M′-M″-X-T_x electronic systems rather than generic metallic conductors. Their interfacial function depends on the specific combination of metal-layer composition, termination chemistry, and atomic arrangement.

3.2. Coupled Regulation of Interfacial Charge Transfer and HER Activity

For photocatalytic H_2 evolution, electron extraction and proton reduction are consecutive processes. An effective MXene cocatalyst must therefore combine rapid semiconductor-to-MXene charge transfer with suitable H* adsorption and H_2 release kinetics. On O-terminated MXenes, H adsorption is mainly governed by the charge state of surface O atoms, while metal composition and layer thickness further affect adsorption energetics and conductivity [112,113]. High conductivity alone is therefore insufficient.

Termination engineering directly regulates this balance. N and S incorporation into $Ti_3C_2T_x$ creates Ti-N and Ti-S environments, reduces charge-transfer resistance, and shifts ΔG_{H^*} toward thermoneutrality [114]. In Mo_2CT_x, mixed O/F terminations moderate the overly strong H adsorption of fully O-terminated surfaces, whereas excessive OH weakens adsorption [115]. Cl/O-terminated $Ti_3C_2T_x$ similarly shows more favorable HER behavior than F/O surfaces, with further improvement after N or S substitution [116]. These results show that terminations regulate HER through both charge redistribution and local bonding.

Metal-layer composition provides complementary control. Co substitution in Mo_2CT_x optimizes H adsorption on neighboring O sites rather than acting only as an isolated active center [117]. Controlled Mo/Nb ordering in $Mo_{2+\alpha}Nb_{2-\alpha}C_3T_x$ likewise changes conductivity and HER activity through long-range electronic redistribution [118].

MXenes can also stabilize highly active catalytic species. Mo vacancies in $Mo_2TiC_2T_x$ anchor Pt single atoms through Pt-C and Pt-O coordination [94]. Ru single atoms and clusters regulate water dissociation and H adsorption [119,120], while expanded $Ti_3C_2T_x$ layers immobilize Pd nanoparticles and improve interfacial electron injection [121]. The MXene therefore serves as a conductive framework, anchoring matrix, and electronic regulator.

This coupled function has been demonstrated in photocatalysis. Br/O-terminated Mo_2CT_x improves charge separation in CdS/Mo_2CT_x while maintaining favorable proton-reduction kinetics, producing 17,566 μmol g^{-1} h^{-1} of H_2 [122]. Rational design should therefore coordinate electron extraction, MXene transport, H* adsorption, and H_2 desorption within the same interface.

3.3. Mo_2TiC_2-Based Interfaces: The $ZnIn_2S_4/Mo_2TiC_2$ Model System

Mo_2TiC_2 provides a representative model for translating metal-layer engineering into photocatalytic function. Our group grew $ZnIn_2S_4$ nanosheets directly on few-layer Mo_2TiC_2 with thicknesses below 1.80 nm. The tightly coupled interface outperformed multilayer, mechanically mixed, and Ti_3C_2-based controls. The optimized $ZnIn_2S_4$/10% Mo_2TiC_2 reached 4.3 mmol g^{-1} h^{-1}, 3.8 times that of $ZnIn_2S_4$ and higher than the corresponding 1%

Pt-loaded system [95]. The enhancement was attributed to Schottky-junction formation, shorter transfer distances, and suppressed electron backflow.

Recent work further shows that $Mo_2TiC_2T_x$ itself can exhibit visible-light-responsive electronic behavior relevant to hydrogen evolution. Delamination enhances the photocurrent response, while optical and electron-energy measurements reveal a band structure compatible with photoinduced reduction. The corresponding absorption, bandgap, and band-edge characteristics are shown in Figure 7 [123].

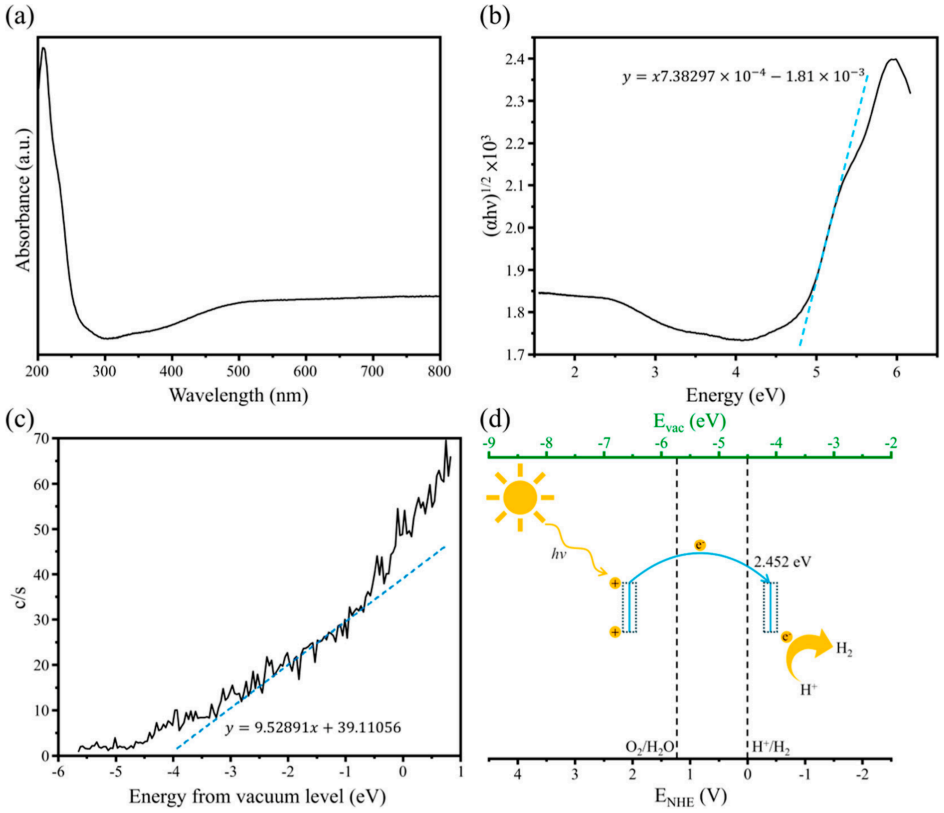

Figure 7. Electronic and optical properties of delaminated $Mo_2TiC_2T_x$: (**a**) UV–visible absorption spectrum; (**b**) Tauc plot, with the blue dashed line indicating the linear extrapolation used to estimate the optical bandgap; (**c**) LEIPS spectrum, with the blue dashed line indicating the linear extrapolation used to determine the onset energy; and (**d**) band-edge diagram showing the energetic positions relevant to hydrogen evolution, where the black vertical dashed lines mark the O_2/H_2O and H^+/H_2 redox potentials [123]. Reproduced from Ref. [123] under CC BY 4.0.

This interface was later extended from electron extraction to temporary storage. In $ZnIn_2S_4/Mo_2TiC_2$-Ru, the Mo_2TiC_2-Ru component receives, stores, and releases photogenerated electrons. This electron-parking behavior suppresses back-transfer and promotes water dissociation and H_2 desorption. The composite produced 5.72 mmol g^{-1} h^{-1} under visible light and retained approximately 1.67 mmol g^{-1} h^{-1} after illumination ceased [124].

The same principle applies to other sulfides. Mo_2TiC_2/ZnCdS achieved 17.73 mmol g^{-1} h^{-1} and an apparent quantum efficiency of 16.22% at 475 nm [96]. Mo_2TiC_2 also improved charge transfer and photocorrosion resistance in $Mn_{0.4}Cd_{0.6}S$ [125] and CdS [126], while $CdIn_2S_4/Mo_2TiC_2$ showed a 55.83-fold enhancement over pristine $CdIn_2S_4$ [97].

Mo_2TiC_2/sulfide interfaces have been described as either Schottky or Ohmic contacts, showing that junction type cannot be inferred from nominal composition alone. Terminations, intercalants, oxidation, work-function matching, morphology, and interfacial bonding can all modify the electronic behavior. Indeed, de-intercalation of $Mo_2TiC_2T_x$ can markedly reduce interflake resistance and shift its apparent transport from semiconductor-like toward

metallic behavior, as shown in Figure 8 [101]. These results highlight the need to relate the actual surface and interface state to charge transfer and reaction kinetics.

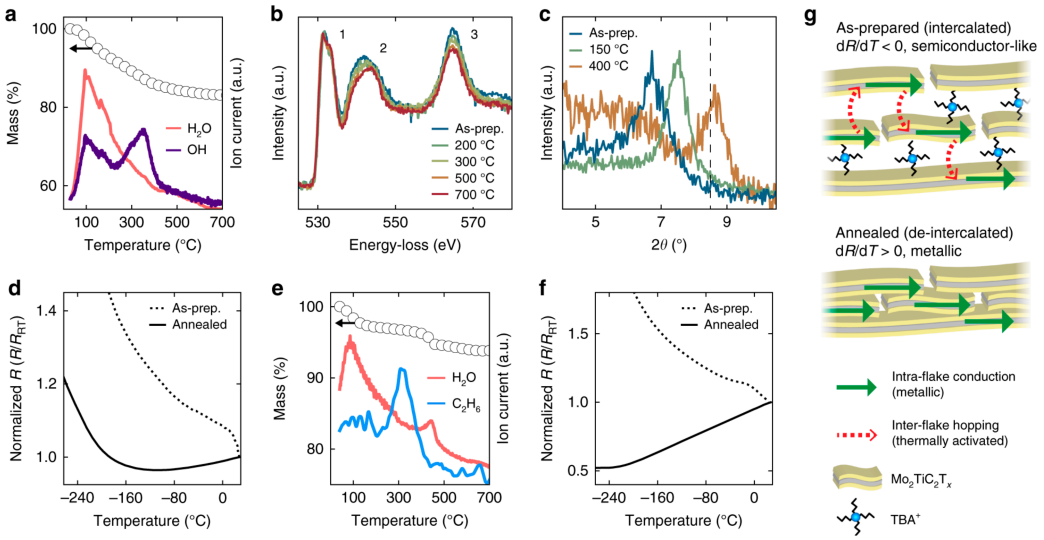

Figure 8. Influence of intercalated species on the structure and electronic transport of Ti_3CNT_x and $Mo_2TiC_2T_x$: (**a**) TGA-MS of Ti_3CNT_x showing the removal of H_2O intercalants and –OH species; (**b**) in situ EELS of the Ti_3CNT_x O K-edge during annealing; (**c**) ex situ XRD of the Ti_3CNT_x (002) peak showing decreased interlayer spacing after annealing; (**d**) temperature-dependent resistance of as-prepared and de-intercalated Ti_3CNT_x; (**e**) TGA-MS of $Mo_2TiC_2T_x$ showing the removal of H_2O and decomposition of TBA+ intercalants; (**f**) temperature-dependent resistance of as-prepared and de-intercalated $Mo_2TiC_2T_x$; and (**g**) schematic illustration of intercalant-controlled conduction in multilayer $Mo_2TiC_2T_x$, highlighting the transition from intercalated semiconductor-like transport to de-intercalated metallic behavior [101]. In (**a**,**e**), the open circles represent the TGA mass data, and the black arrows indicate the corresponding left y-axes. The vertical dashed line in (**c**) marks the reference position of the Ti_3CNT_x (002) peak after annealing at 150 °C. In (**d**,**f**), the dotted and solid lines represent the as-prepared and annealed samples, respectively. In (**g**), the red dashed arrows indicate thermally activated interflake hopping. Reproduced from Ref. [101] under CC BY 4.0.

4. Precision Design of MXene Photocatalytic Interfaces

Although this review focuses on photocatalytic H_2 evolution, selected non-H_2 systems are included where they reveal transferable MXene interfacial functions that are difficult to isolate in conventional H_2-evolution systems. These examples are used to clarify electric-field regulation, carrier selectivity, multimetallic-site cooperation, and reaction-specific adsorption rather than as direct benchmarks for H_2 production.

4.1. Working-State Surface Chemistry and Precise Termination Control

Having established how surface terminations regulate electronic structure and HER activity, the next challenge is to control and identify these terminations under realistic synthesis and working conditions. Precise termination engineering requires control over termination identity, coverage, adsorption site, and spatial arrangement rather than reliance on nominal T_x composition. Conventional aqueous etching usually produces heterogeneous O/OH/F surfaces containing intercalated water and residual ions, so the measured properties reflect intrinsic electronic states, interlayer transport, and surface chemistry simultaneously [101]. Postsynthetic covalent exchange has expanded the accessible terminations to NH, S, Cl, Se, Br, and Te [40], while ordered O-B-O layers show that termination arrangement can be as important as elemental identity [127]. Realistic mixed surfaces further exhibit non-additive changes in stability and electronic structure [102].

These limitations have driven synthesis toward better-defined surfaces. Lewis-acid etching, controlled halogenation, and direct growth enable Cl-rich, uniformly terminated, and mixed-halogen MXenes [38,103,111]. Electrochemical etching in dilute HCl produced fluoride-free Ti_2CT_x containing O, OH, and Cl species [128], whereas molten salts yielded nearly saturated Cl terminations on Ti_2C and Ti_3C_2 and were later extended to broader MAX precursors [39,129]. Molten-salt-assisted electrochemical synthesis further enabled the conversion of Cl terminations into O- or S-containing surfaces [130].

Termination formation remains sensitive to both the MXene backbone and reaction environment. Calculations show that a species stable under one condition may be replaced or oxidized under another [131]. Operando XRD further revealed that molten-salt etching proceeds through lattice expansion, transient phases, termination grafting, and eventual over-etching [132]. Direct gas-phase synthesis offers a more defined alternative by forming the lattice and termination simultaneously. Yue et al. [133] prepared few-layer, single-phase Ti_2CCl_2 and Ti_2NCl_2 in one step, avoiding conventional etching and post-delamination. Figure 9 summarizes the synthesis route and structural evidence for phase-pure, Cl-terminated MXenes with layered morphology and high stability [133].

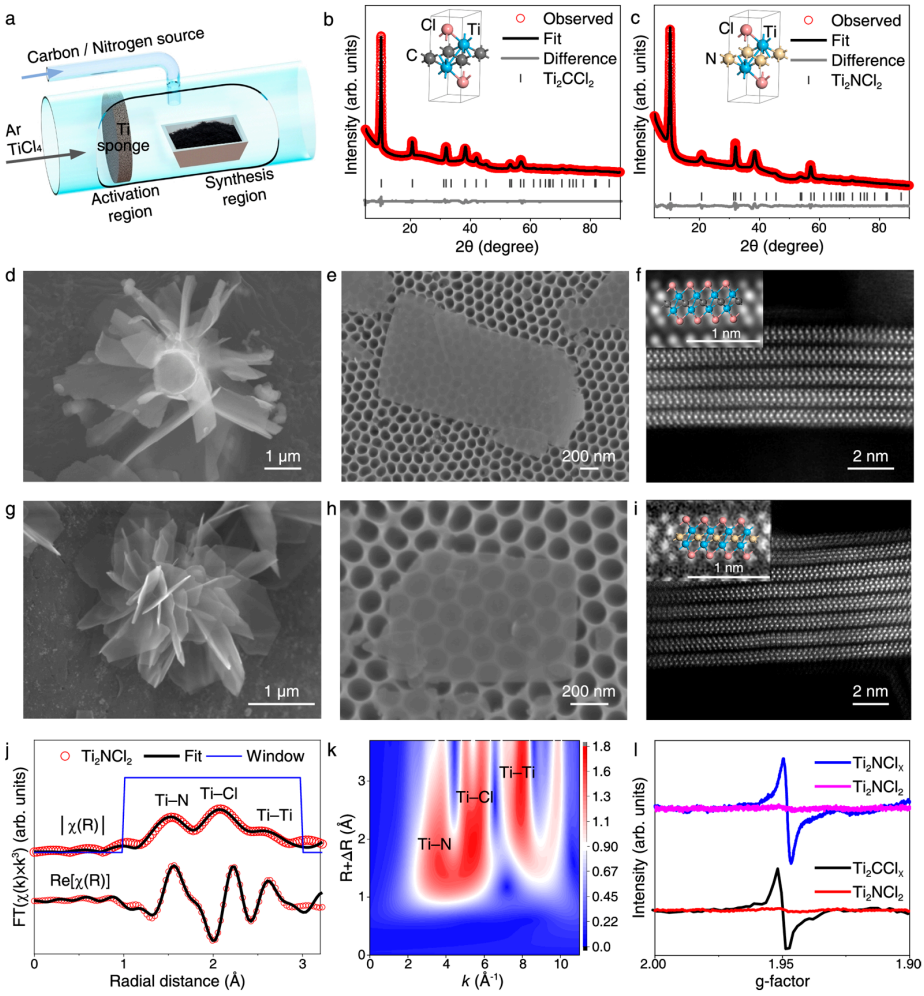

Figure 9. (**a**) Schematic diagram of the one-step gas-phase reactor. (**b**,**c**) XRD patterns and Rietveld refinements of Ti_2CCl_2 and Ti_2NCl_2. (**d**,**e**) SEM images of directly synthesized and dispersed Ti_2CCl_2. (**f**) Atomic-resolution HAADF-STEM image of Ti_2CCl_2. (**g**,**h**) SEM images of directly synthesized and dispersed Ti_2NCl_2. (**i**) Atomic-resolution HAADF-STEM image of Ti_2NCl_2. (**j**,**k**) EXAFS fitting and wavelet-transform analysis of Ti_2NCl_2. (**l**) EPR spectra of directly synthesized and etching-derived MXenes [133]. Reproduced from Ref. [133] under CC BY 4.0.

Reliable surface identification is equally important. Thermal or H_2 treatment can remove existing terminations and enable retermination [134], while heating redistributes O and F among nonequivalent sites [135]. UPS/XPS identified Ti-F hybridization and different O adsorption sites but found limited evidence for intrinsic OH on impurity-minimized $Ti_3C_2T_x$ [136]. Solid-state NMR, however, detected OH- and H_2O-related environments in conventionally prepared samples [137]. Adsorbed water, surface oxides, residual phases, and handling effects may therefore be mistaken for intrinsic terminations, requiring surface- and bulk-sensitive signals to be distinguished [138].

The working surface may also differ from the as-synthesized state. H_2O can bind at Ti-Ti bridge sites and behave as an additional termination species [88], while photoexcitation can alter the stability of F, O, OH, H, halogen, and chalcogen terminations [139]. Surface reduction may further couple termination removal with electron injection and subsequent O/OH recoordination [140].

Precise termination design should therefore integrate controlled synthesis, reliable surface identification, and working-state verification. The relevant target is not the nominal $M_{n+1}X_nT_x$ composition, but the termination distribution and local coordination retained under photocatalytic conditions.

4.2. MXene Quantum Dots for Nanoscale Interface and Electric-Field Regulation

Reducing MXenes from two-dimensional sheets to quantum dots creates spatially dispersed interfacial regulators. Their small size, high dispersibility, exposed edges, and rich surface chemistry increase contact density, shorten transfer distances, and reduce light shielding. In g-C_3N_4/Ti_3C_2 QD composites, the optimized system reached 5111.8 μmol g^{-1} h^{-1}, approximately ten times the activity of the corresponding Ti_3C_2-sheet composite [141]. Ti_3C_2 QDs have also been incorporated into $BiVO_4$@$ZnIn_2S_4$ direct Z-scheme [142] and TiO_2/g-C_3N_4 S-scheme systems [143], where they extract electrons and provide additional reduction sites without disrupting the primary transfer pathway.

Their function can be further tuned through defects, doping, and terminations. Partially reduced Ti_3C_2 QDs contain Ti^{3+} and oxygen-vacancy sites that combine electron trapping with reactant activation [144]. Nitrogen doping strengthens coupling with CdS nanorods and increases the H_2 evolution rate to 17.09 mmol g^{-1} h^{-1} [98]. More selective carrier routing was achieved by coloading O-terminated Ti_3C_2 QDs and N-doped carbon dots on CdS, where the two components acted as electron- and hole-accepting units, respectively, giving 5.64 mmol g^{-1} h^{-1} and an apparent quantum efficiency of 45.7% at 450 nm [145]. Ti_3C_2 QDs may also provide photothermal promotion, although this contribution should be separated from charge-transfer effects [99].

A more distinctive function of nanoscale MXene interfaces is local electric-field regulation. A recent non-H_2 system provides direct evidence for this principle. At a Cl-terminated MXene/perovskite interface, MXene-induced dipoles modified the local work function and generated n-type character at the buried interface. Combined with an opposite surface potential gradient, this produced dipole-driven band bending that promoted carrier extraction and suppressed recombination, as shown in Figure 10 [146]. In Figure 10a, the differently colored spheres distinguish the atomic species in the MX-Cl/$MAPbI_3$/4-FPEAI interface, while the red arrows indicate interfacial work-function shifts. In Figure 10b, the horizontal and vertical arrows in the insets indicate the short-circuit current density (JSC) and open-circuit voltage (VOC), respectively. Although demonstrated in a photovoltaic interface, this result provides a transferable model for understanding how MXene surface chemistry and spatial confinement can regulate local electrostatic fields.

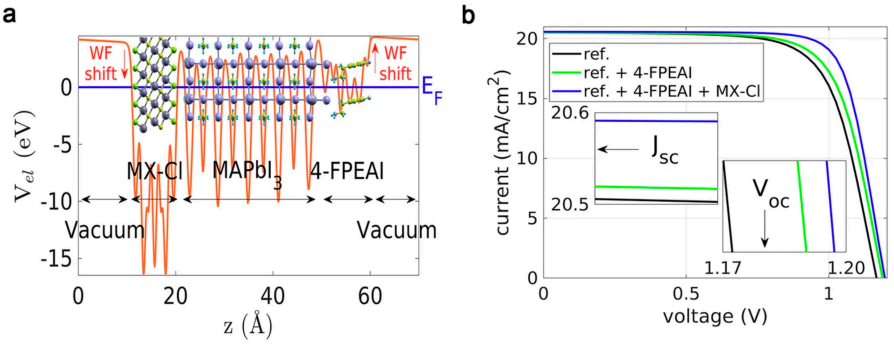

Figure 10. MXene-induced interfacial field-effect regulation: (**a**) optimized atomic structure of the MX-Cl/$MAPbI_3$/4-FPEAI interface and the corresponding plane-averaged electrostatic-potential profile, showing asymmetric interfacial work functions; and (**b**) simulated J–V characteristics of the reference, 4-FPEAI-modified, and MX-Cl/4-FPEAI devices, with corresponding JSC and VOC values [146]. Reproduced from Ref. [146] under CC BY 4.0.

This field-engineering principle is directly relevant to photocatalytic MXene QDs. The Nb_2C QD/COF system further demonstrated that highly dispersed QDs can act as nanoscale dipoles rather than simple electron sinks. The QDs strengthened the built-in electric field, accelerated charge separation, and optimized O_2 adsorption, enabling sacrificial-agent-free H_2O_2 production from air and seawater [147]. KPFM, light-induced XPS, transient absorption, and theoretical calculations linked the interfacial potential difference with carrier kinetics and reaction energetics, as shown in Figure 11.

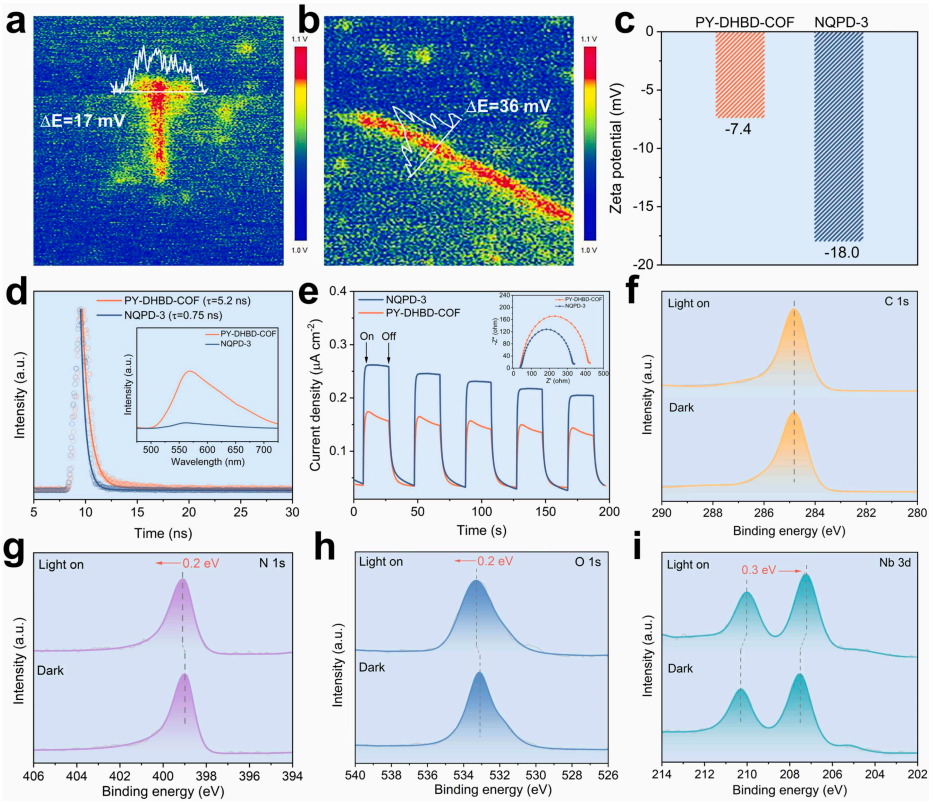

Figure 11. (**a**,**b**) Surface potentials of PY-DHBD-COF and NQPD-3 measured by KPFM. (**c**) Zeta potentials of PY-DHBD-COF and NQPD-3. (**d**) Photoluminescence and time-resolved photoluminescence spectra. (**e**) EIS Nyquist plots and transient photocurrent-response curves. (**f**–**i**) In situ light-irradiation XPS spectra of NQPD-3. In (**g**–**i**), the red arrows indicate the light-induced binding-energy shifts of N 1s (−0.2 eV), O 1s (−0.2 eV), and Nb 3d (+0.3 eV), respectively [147].

Recent multicomponent systems extend MXene QDs from terminal acceptors to electronic relays. In $Ni_2P/Zn_{0.5}Cd_{0.5}S@Ti_3C_2$ QDs, the QDs facilitate electron transport, while Ni_2P provides the main HER sites [148]. Ti_3C_2 QDs have also been coupled with $BaTiO_3$ polarization fields, combining piezoelectric charge separation with QD-mediated electron extraction [149].

Dimensional reduction, however, simultaneously changes size, terminations, defect density, oxidation state, and work function. Improved performance should therefore not be attributed to quantum confinement alone. Reliable identification requires matched sheet/QD controls together with work-function measurements, KPFM, light-induced spectroscopy, ultrafast dynamics, and charge-density calculations. The design objective is to use MXene QDs as distributed electronic nodes that integrate short-range charge extraction with local field and active-site regulation.

4.3. Emerging Compositionally Complex MXenes for Cooperative Active-Site Design

Solid-solution MXenes extend composition control beyond discrete single- and double-metal structures. In Ti_2-gammaNbgammaCT_x, Ti_2-gammaVgammaCT_x, and V_2-gammaNbgammaCT_x, continuous M-site substitution produces composition-dependent changes in conductivity and optical absorption [150]. TiVCT_x and $Mo_xV_{4-x}C_3T_x$ further show that the metal ratio also affects termination chemistry and surface redox behavior [151,152]. Similar Nb-containing solid solutions confirm that transport, surface chemistry, and stability can be regulated through composition [153].

High-entropy MXenes further broaden this space by integrating multiple transition metals within one lattice. Four-metal TiVNbMoC_3T_x and TiVCrMoC_3T_x established the feasibility of high-entropy atomic layers [154], followed by five-metal M_2CT_x, $M_4C_3T_x$, and $M_5C_4T_x$ structures with wider distributions of local coordination and strain [155,156]. Medium-entropy $Ti_{1.1}V_{1.1}Cr_{0.4}Nb_{1.4}C_3T_x$ also shows that stable complex compositions need not be equimolar [157]. The objective should therefore be reaction-specific composition design rather than simply increasing the number of metals.

Average composition alone does not define the active surface. Controlled Mo/Nb occupation in $Mo_{2+\alpha}Nb_{2-\alpha}C_3T_x$ changes both conductivity and HER activity [118]. Entropy-driven transitions from short-range order to greater disorder have also been observed in multimetallic carbides [158], while high-entropy MXenes may contain multihyperuniform arrangements that differ from ideal random models [159]. Active-site models must therefore consider local ordering, segregation, and coordination.

The catalytic value of compositional complexity lies in combining neighboring sites with complementary functions. In Ti-V-Mo-Cr high-entropy MXenes, different local environments provide a distribution of H* adsorption strengths. Short-range Mo ordering creates favorable migration pathways, allowing H spillover between strong- and weak-binding sites and lowering the Volmer–Tafel barrier [160]. High-entropy MXenes can also regulate supported catalytic centers. In V-Co_2P/high-entropy MXene interfaces, electronic coupling optimizes water and intermediate adsorption, and lowers the barriers of both HER and OER [161].

The VNbC/COF system provides a photocatalytic example. Alloyed V-Nb sites promoted interfacial charge transfer and strengthened styrene adsorption, enabling nearly complete conversion with 99% epoxide selectivity during coupled H_2O_2 photosynthesis and alkene epoxidation [162]. The VNbC/COF structure and cooperative V-Nb sites are shown in Figure 12. This result demonstrates that compositionally complex MXenes can coordinate carrier transfer and reaction-specific adsorption rather than merely increase the number of nominal active sites.

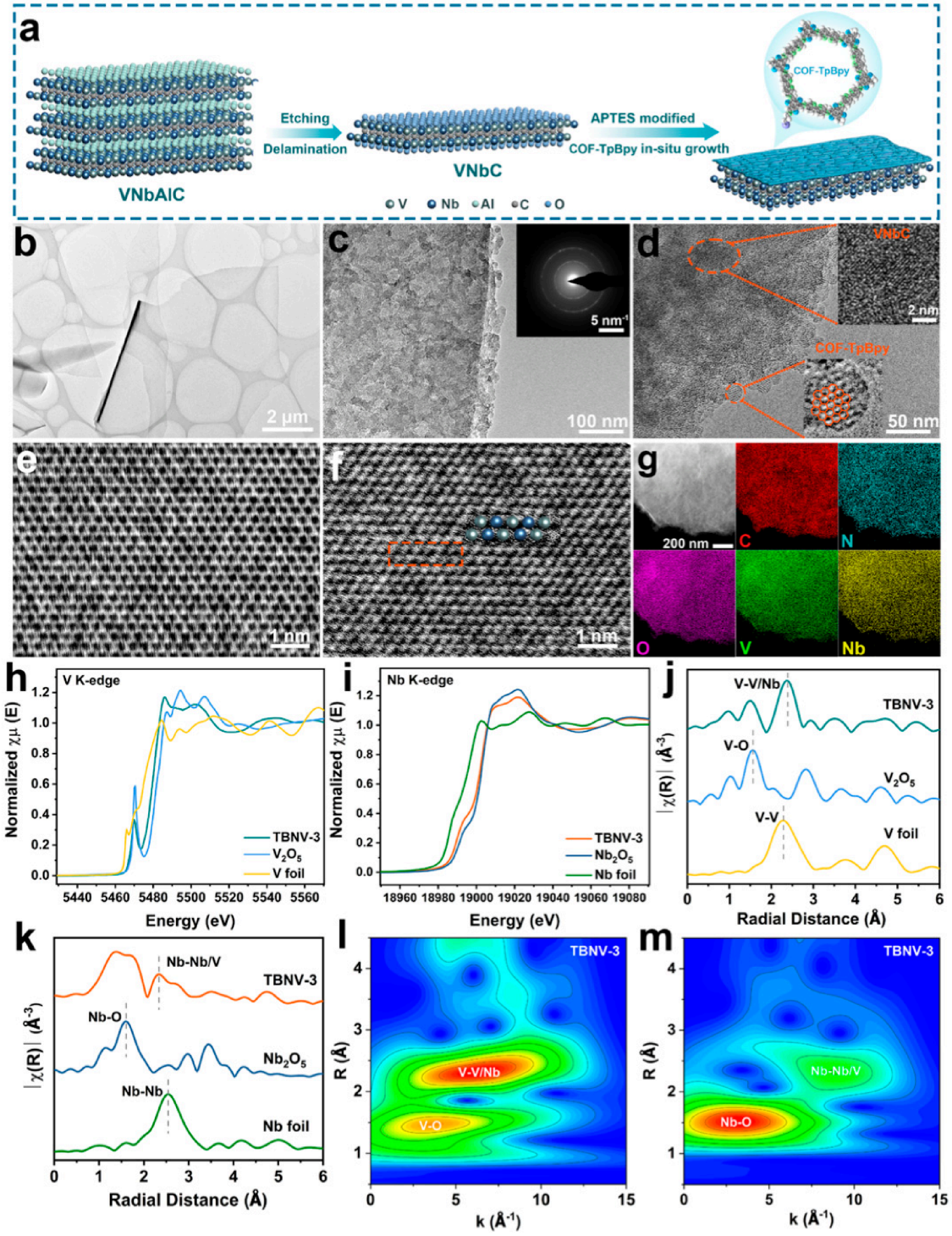

Figure 12. (**a**) Schematic illustration of the synthesis of COF-TpBpy@VNbC, where the dark-green, dark-blue, light-green, gray, and blue spheres represent V, Nb, Al, C, and O atoms, respectively. (**b**) TEM image of VNbC. (**c**) TEM image of TBNV-3, with the inset showing the selected-area electron diffraction (SAED) pattern. (**d**) HRTEM image of TBNV-3, where the orange dashed outlines highlight the VNbC and COF-TpBpy regions. (**e**) Aberration-corrected STEM and **(f)** HAADF-STEM images of VNbC, with the orange dashed box in (**f**) highlighting the local atomic arrangement. (**g**) EDX elemental mappings of TBNV-3, with C, N, O, V, and Nb shown in red, cyan, purple, green, and yellow, respectively. (**h**,**i**) XANES and (**j**,**k**) EXAFS spectra of TBNV-3 and the reference samples. Wavelet-transform EXAFS plots at the (**l**) V K-edge and (**m**) Nb K-edge, where the color scale from blue to red indicates increasing signal intensity [162].These systems also illustrate how MXene composition shifts the dominant interfacial function. $Ti_3C_2T_x$ provides the classical termination-sensitive platform

for electron extraction and transport [43], whereas Mo_2TiC_2 couples multimetallic electronic regulation with H-adsorption control [123]. At reduced dimensions, Nb_2C QDs can act as local dipoles that strengthen interfacial electric fields [147], while VNbC introduces cooperative multimetallic sites for carrier transfer and reaction-specific adsorption [162]. These distinctions are not intrinsic labels, however, because the observed role also depends on termination state, dimensionality, semiconductor partner, and reaction environment. Direct applications of high-entropy MXenes in photocatalytic H_2 evolution remain limited. Future work should identify defined local ensembles for electron extraction, adsorption, intermediate migration, and bond activation using atomic-resolution mapping, operando spectroscopy, and calculations based on realistic metal and termination distributions. The principal structure-encoded variables and their functional consequences are summarized in Table 3.

4.4. Reaction-Specific Role Design and AI-Assisted Materials Discovery

MXene cocatalysts should be designed for the target reaction rather than assigned a fixed electron-sink role. Replacing sacrificial donors with productive oxidation reactions enables simultaneous use of photogenerated electrons and holes. $Ti_3C_2T_x$/CdS, for example, couples H_2 evolution with the selective oxidation of furfuryl alcohol to furfural [163]. Figure 13 shows the coupled reaction pathway, the dependence of product yields and substrate conversion on $Ti_3C_2T_x$ content, and the cycling stability of the optimized composite [163]. CdS-$Ti_3C_2T_x$ similarly integrates H_2 evolution with bioethanol conversion to 1,1-diethoxyethane [164], while MXene/$Zn_xCd_{1-x}S$ combines H_2 production with PET degradation [165]. In these systems, the MXene function is defined within the complete redox process rather than by proton reduction alone.

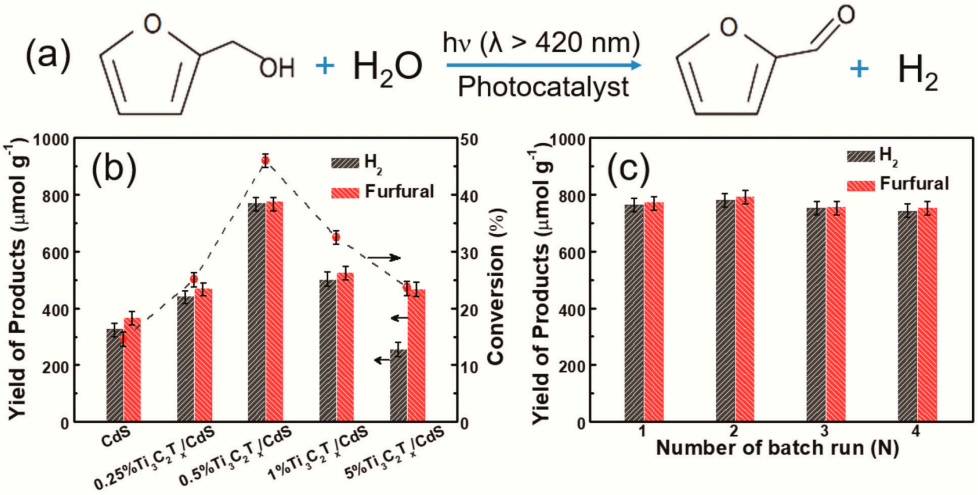

Figure 13. (**a**) Photocatalytic conversion of furfuryl alcohol to furfural coupled with H_2 evolution, with the arrow indicating the reaction under visible-light irradiation. (**b**) Product yields and furfuryl-alcohol conversion over CdS and $Ti_3C_2T_x$/CdS composites with different $Ti_3C_2T_x$ contents under visible-light irradiation for 4 h, where the left-pointing arrows indicate the H_2 and furfural yields corresponding to the left y-axis, and the right-pointing arrow indicates furfuryl-alcohol conversion (dashed line) corresponding to the right y-axis. (**c**) Recycling performance of 0.5% $Ti_3C_2T_x$/CdS [163].

Table 3. Structure-encoded design variables and their functional consequences in MXene cocatalysts.

Design Variable	Structural Implementation	Primary Electronic/Interfacial Effect	Cocatalytic Consequence	Key Descriptors for Comparison	Representative Refs.
Metal-layer composition and atomic ordering	Select outer/inner transition-metal layers and control layer-resolved occupation in ordered double-transition-metal MXenes.	Reconstructs d states near the Fermi level, conductivity, metal–termination orbital coupling, and adsorption energetics.	Couples rapid electron transport with tunable H* binding; separates backbone transport from surface-reaction functions.	Work function, DOS and orbital occupation; d-band descriptor, ΔG_{H^*}, and layer-order parameter.	[104,106,118]
Solid-solution and medium/high-entropy composition	Continuous M-site substitution or multimetal lattices with controlled short-range order rather than assuming an ideal random alloy.	Creates distributions of local coordination, charge, strain, and adsorption energies that are not captured by average composition.	Enables complementary strong- and weak-binding sites, H* migration/spillover, and reaction-specific local ensembles.	Local composition and pair correlations, short-range-order parameter, strain distribution, ΔG_{H^*} distribution, and migration barrier.	[150,154,158,160,166]
Termination identity, coverage, and spatial distribution	Regulate O, OH, F, Cl/Br and other anionic terminations; control mixed-surface ratios and adsorption sites.	Changes surface dipoles, work function, charge redistribution, metal–T_x bonding, and interfacial band alignment.	Tunes electron/hole selectivity, back-transfer suppression, water/proton interaction, and H* adsorption strength.	Termination coverage and site occupancy, work function, surface potential, Bader charge, ΔG_{H^*}, and termination stability.	[101,114–116]
Thickness, dimensionality, and synthesis/processing route	Control layer number, lateral size, delamination, direct CVD growth, or one-step gas-phase formation.	Modulates sheet and interflake resistance, carrier-scattering length, accessible area, oxidation susceptibility, and contact geometry.	Controls extraction distance, density of interfacial nodes, light shielding, and batch-to-batch reproducibility.	Layer number, lateral size, conductivity, interflake resistance, oxidation fraction, and effective interface area.	[61,110,111,133]
Vacancies and substitutional sites	Introduce metal/cation vacancies, second-shell defects, or isolated substitutional metals while retaining the MXene framework.	Produces local coordination asymmetry, charge polarization, anchoring sites, and modified reactivity of neighboring terminations.	Can strengthen interfacial fields, stabilize single atoms, and tune adjacent O-terminated HER sites without making the dopant the direct H* site.	Defect formation energy, coordination number, Bader charge, local DOS, and vacancy concentration and spatial distribution.	[92,117]
Supported single atoms, clusters, and nanoparticles	Immobilize Pt or Ru single atoms, Ru clusters, or Pd nanoparticles through MXene C/O/heteroatom coordination.	Generates metal–support charge transfer, suppresses aggregation, and differentiates water-dissociation and hydrogen-binding sites.	Adds kinetically specialized centers for water activation, H* formation, recombination, and H_2 desorption.	M–C/O coordination; oxidation state, dispersion, metal loading, water-dissociation barrier, and ΔG_{H^*}.	[94,119–121]

Reaction-specific design can also extend MXene functions toward oxidation. In La-MOF@MXene, interfacial electron withdrawal shifts the valence-band position and promotes hole migration [167]. Ti_3C_2 can likewise serve as a hole-transfer and accumulation component in an appropriately aligned MOF interface [168]. Our VNbC/COF system combines carrier transport with styrene adsorption and selective epoxidation [162], while Nb_2C QDs regulate the built-in electric field and O_2 reduction pathway during COF-based H_2O_2 production [147]. MXenes can therefore be tailored to regulate carrier transfer, reactant adsorption, and intermediate conversion according to the required reaction sequence.

The growing combinations of metal layers, terminations, defects, and interfaces make exhaustive experimental screening impractical. Early data-driven studies screened ordered binary MXenes using stability, conductivity, and hydrogen-adsorption free energy, while identifying geometric and elemental descriptors for HER activity [109]. Machine-learning and DFT workflows later predicted hydrogen-adsorption free energies across 4500 $MM'XT_2$ configurations [169]. For CO_2 activation, interpretable models identified the d-band center, surface-metal electronegativity, and valence-electron count as key descriptors [170]. These approaches accelerate screening but remain largely focused on isolated adsorption properties.

Photocatalysis-oriented screening requires broader criteria. Janus MXenes with asymmetric metal layers or terminations can generate intrinsic dipoles, realign band edges, and spatially separate reduction and oxidation reactions [171]. The MXgap model predicts metallic or semiconducting behavior and bandgaps, enabling rapid selection based on optical absorption and band alignment [172]. Deep-learning screening has further incorporated thermodynamic stability, band alignment, light absorption, carrier effective masses, and nonadiabatic electron–hole recombination [173]. Figure 14 presents the screened composition and termination space, four representative MXene configurations, and the high-throughput workflow used to evaluate 23,857 structures and identify 14 candidate photocatalysts [173].

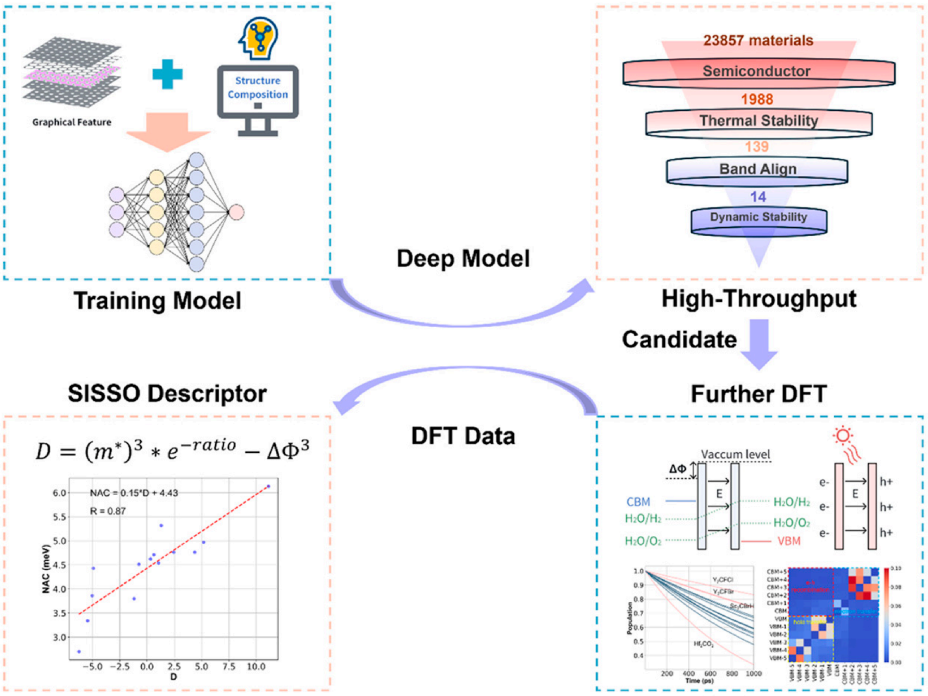

Figure 14. Deep learning-enabled high-throughput screening of MXene photocatalysts, integrating stability prediction, band alignment, light absorption, carrier properties, nonadiabatic electron–hole recombination, and built-in electric-field evaluation [173].

Reaction-specific discovery must also consider multiple intermediates and realistic local environments. Models covering H_2O, CO_2, CO, H_2, O_2, OH, O, and H adsorption show that different species and terminations can be treated within a common predictive framework [174]. In high-entropy $TiVNbMoC_3O_2$, H adsorption depends mainly on the first-neighbor metal environment around surface O sites rather than on average composition. Machine learning further identified the mean covalent radius of neighboring metals as an effective local descriptor [166]. Future models should therefore represent adsorption-site geometry, local coordination, termination distribution, and competing intermediates.

AI-assisted MXene discovery should therefore be reaction-defined and multiobjective, considering charge-transfer direction, adsorption energetics, kinetic barriers, selectivity, stability, and light absorption. Candidate structures must ultimately be verified under working conditions because reconstruction, oxidation, solvent adsorption, and charge redistribution may alter their predicted functions. The goal is to connect target reactions with experimentally verifiable MXene interfacial roles.

5. Conclusions and Perspectives: Toward Programmable MXene Interfacial Cocatalysts

The preceding sections show that MXene cocatalytic functions emerge from the interplay of electronic structure, interfacial coupling, surface chemistry, dimensionality, and reaction conditions. This section therefore consolidates these mechanistic insights, identifies unresolved questions under working conditions, and outlines a path toward reaction-specific and programmable MXene interfacial cocatalysts.

5.1. Mechanistic Convergence and Role Diversification

The $Ti_3C_2T_x$ electron-sink model remains the starting point for understanding MXene-assisted photocatalytic H_2 evolution. In early metal-sulfide/Ti_3C_2 systems, Fermi-level equilibration, conductive transport, and O-terminated HER sites jointly enabled electron extraction, transfer, and proton reduction [43]. An effective MXene cocatalyst must therefore connect charge separation with surface electron consumption rather than act only as a conductive additive.

This role is conditional rather than universal. In $ZnIn_2S_4/Mo_2TiC_2$, metal-layer composition and local coordination regulate both electron extraction and H adsorption [123]. Our VNbC/COF system further shows that multimetallic sites can couple carrier transfer with reaction-specific adsorption [162]. Terminations, defects, and interfacial bonding can therefore reshape work functions, orbital coupling, and adsorption energetics [93].

MXenes may consequently receive, transport, store, or consume charge. Suitable band alignment can promote hole transfer instead of electron extraction [168]. Vacancies can stabilize isolated HER centers [94], while Mo_2TiC_2-Ru enables temporary electron storage and delayed release [124]. MXene quantum dots can further regulate local electric fields and reactant activation [146,147].

MXenes should therefore be defined by their working interfacial function rather than nominal composition. Their dominant role depends on the structure of the interface and the rate-limiting step of the target reaction.

5.2. Unresolved Questions in Working-State MXene Interfaces

A central uncertainty is whether the characterized structure represents the interface operating during photocatalysis. Water, pH, temperature, illumination, and adsorbates can alter terminations, coordination, and oxidation states. $Ti_3C_2T_x$ readily oxidizes in liquids [175], particularly under acidic or heated conditions [176]. Water can also adsorb on

surface Ti, weaken Ti-C bonds, dissociate, and extract Ti atoms [177]. The working surface may therefore differ substantially from the nominal O/OH/F structure [88,139].

Dynamic surface chemistry also complicates charge-transfer assignment. Similar Mo_2TiC_2/sulfide interfaces have been described as either Schottky or Ohmic contacts [123,125]. In situ KPFM further shows that high-work-function MXenes favor electron acceptance, whereas OH-rich surfaces may promote hole transfer [178]. Nominal composition, PL quenching, photocurrent, or impedance alone cannot establish the carrier pathway.

The catalytic site is equally uncertain. H* adsorption may occur on O terminations [112], while substitutional metals can regulate neighboring O sites [117]. Vacancies may anchor isolated metals [94], and adsorbed water, exposed metal atoms, reconstructed O/OH species, or oxide phases may also participate [88,140]. Electron accumulation on MXene therefore does not identify the proton-reduction site.

Surface quantification introduces further ambiguity. XPS signals may contain contributions from terminations, water, oxides, residual phases, and adventitious species [136,137]. Conventional analysis can overestimate Ti vacancies and underestimate terminal atoms, particularly F [179]. Reliable assignment requires corrected XPS combined with XAS, NMR, SIMS, or atomic-resolution microscopy.

Practical evaluation presents a separate challenge. Many high-performing MXene photocatalysts still rely on sacrificial donors and Cd-based sulfides, so high mass-normalized H_2-evolution rates do not directly translate to overall water splitting or scalable solar H_2 production. Meaningful comparison therefore requires standardized reporting of photon flux, catalyst loading, AQY/AQE, long-term stability, and post-reaction MXene composition. Solar-to-hydrogen efficiency should be used when true overall water splitting is demonstrated, rather than being extrapolated from sacrificial-agent-assisted H_2 evolution.

Because synthesis and processing often alter multiple variables simultaneously, future studies should use matched controls to connect the as-synthesized structure with working-state reconstruction, local potential, carrier dynamics, intermediates, and products. The central question is which evolving structure performs each interfacial function under reaction conditions. The corresponding validation requirements are summarized in Table 4.

5.3. Design Roadmap Toward Programmable Cocatalytic Platforms

Programmable MXene cocatalysts should be designed from the target reaction. Required functions such as carrier extraction, back-transfer suppression, adsorption, intermediate stabilization, and product desorption can be encoded through metal composition, terminations, defects, dimensionality, and interfacial bonding [40,103,127,147,158]. Their successful design ultimately requires verification under working conditions.

Reliable design requires structure–function relationships under operating conditions. Static models cannot capture termination reconstruction, oxidation, solvent adsorption, or changes in interfacial potential. Computational screening should therefore be combined with corrected surface analysis, operando spectroscopy, and local-potential measurements [173,178,179]. AI-ready datasets should link synthesis, structure, spectra, reaction conditions, negative results, and uncertainty [180].

Closed-loop experimentation provides a practical route through this design space. A mobile robotic platform completed 688 photocatalytic experiments and identified a formulation with sixfold higher activity [181]. Machine learning-guided screening also enriched active candidates within large ternary heterojunction libraries [182]. For MXenes, optimization should include efficiency, selectivity, stability, oxidation resistance, and reproducibility rather than H_2 evolution rate alone.

Table 4. Working-state questions, minimum evidence requirements, and validation criteria for assigning MXene interfacial roles.

Working-State Question	Major Confounding Factors	Minimum Evidence Set	Acceptable Validation Criterion	Representative Refs.
Does the MXene remain structurally intact during photocatalysis?	Water, dissolved O_2, pH, temperature, irradiation, and defects can oxidize or dissolve the carbide and generate electronically coupled oxide phases.	Time-resolved or operando structural/chemical-state measurements, supported by pre/post-reaction XRD, Raman, XPS/XAS, TEM, and dissolved-metal analysis.	Distinguish intact MXene from partially oxidized MXene and MXene-derived $TiO_2/NbO_x/MoO_x$; stability cannot be inferred from activity retention alone.	[175–177]
What are the identity, coverage, and adsorption sites of the working terminations?	Intrinsic terminations overlap with adsorbed/intercalated water, surface oxides, etching residues, and adventitious species; heating and photoexcitation can redistribute them.	XPS/UPS combined with at least one chemically independent probe such as solid-state NMR, XAS, controlled desorption, or atomic-resolution microscopy; report fitting constraints and uncertainty.	Assign termination identity, coverage, site occupancy, and environmental dependence rather than describing the surface only as nominal O/OH/F-T_x.	[88,135–139]
Does an irradiated-XPS binding-energy shift establish charge-transfer direction and magnitude?	Differential charging, surface photovoltage, final-state screening, calibration choices, and peak-fitting variability can mimic or modify shifts.	Paired dark/light spectra with internal calibration and repeated measurements, integrated with work-function/band-alignment data and an independent spatial or time-resolved carrier probe.	Use irradiated XPS as one element of a convergent evidence chain; do not derive transferred-electron numbers or a junction type from peak shifts alone.	[86]
Which working-state site actually performs proton reduction?	Surface O/OH, exposed metal atoms, vacancies, supported species, adsorbed water, or reconstructed oxides may all bind H*; electron accumulation does not identify the active site.	Calculations on realistic mixed/reconstructed surfaces plus site-sensitive experiments, such as isotope labeling/KIE, selective poisoning, operando vibrational or XAS measurements, and rate correlation.	Connect the proposed site to a specific intermediate and elementary step, and explain activity changes under matched site perturbations.	[112,113]
Does synthesis or operation induce phase and termination reconstruction?	Molten-salt etching, over-etching, reduction, retermination, and electron injection can generate transient phases and surfaces absent from the nominal starting material.	Operando or time-resolved phase/chemical-state tracking, quenched intermediate samples, and mass/composition balance across initial, intermediate, and working states.	Establish a continuous pathway linking the initial structure, intermediate states, and working structure before assigning the catalytic role to the as-synthesized phase.	[132,140]

Working-state characterization should be integrated into this feedback loop. Operando quick XAS combined with machine learning has resolved dynamic coordination and phase evolution [183], illustrating how working-state information can refine theoretical models and guide subsequent synthesis.

Active learning is well suited to the limited and heterogeneous datasets available for MXenes.

The A-Lab synthesized 36 of 57 targeted inorganic compounds by integrating computation, literature knowledge, robotics, characterization, and active learning [184]. Another closed-loop study identified a high-performing four-metal catalyst from 30 initial samples and ten additional experiments [185]. These closed-loop platforms have not yet reached comparable maturity for MXene photocatalysts and are discussed here as transferable methodological models rather than established MXene-specific workflows. MXene datasets should therefore record terminations, oxidation states, interlayer species, morphology, and interface quality together with composition.

Programmability must finally survive scale-up. Automated screening of molecular nanojunction photocatalysts was transferred to continuous-flow production at approximately 200-fold scale, as shown in Figure 15 [186]. Similar translation for MXenes will require reproducible etching, delamination, termination control, semiconductor growth, and oxidation management.

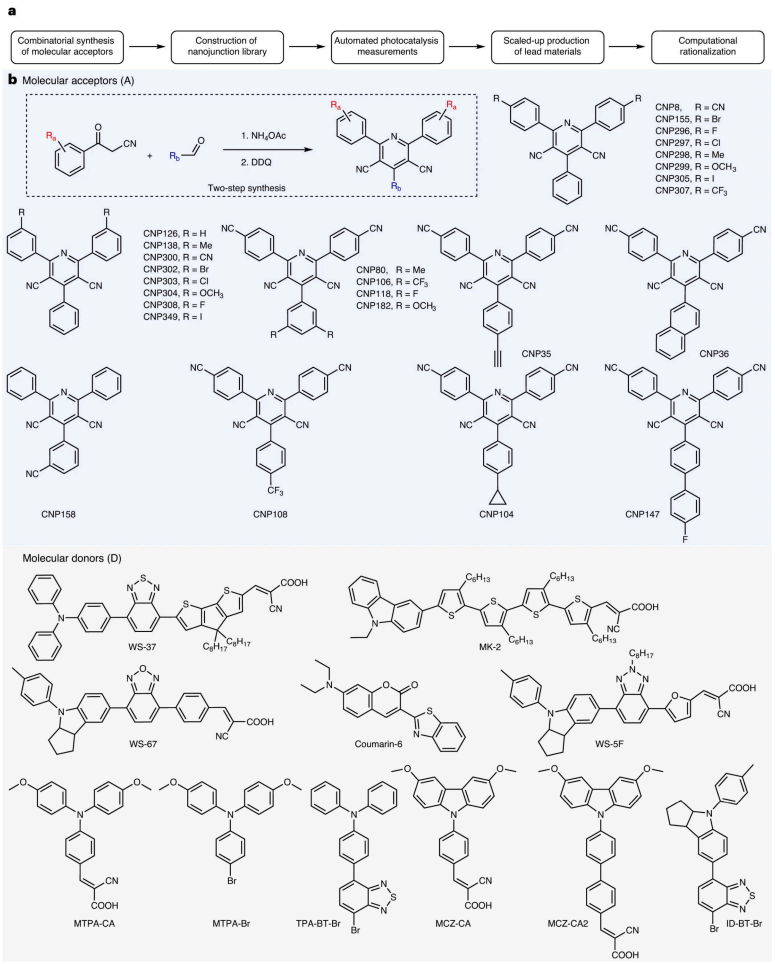

Figure 15. (**a**) Pipeline for the accelerated discovery, scale-up production, and computational rationalization of molecular nanojunction photocatalysts. (**b**) Chemical structures of the molecular acceptors and donors used to construct the combinatorial library [186]. Reproduced from Ref. [186] under CC BY 4.0.

A practical design strategy should connect reaction requirements with controllable structural variables, working-state verification, and multiobjective optimization before scale-up. Programmable MXene cocatalysis will depend not on reporting more materials, but on reproducibly controlling defined interfacial functions for specific reactions.

Author Contributions: Y.S. and Y.L. conducted the literature search and wrote the first draft of the manuscript; J.M., Q.Z., Y.W., Y.H., M.Z., H.Z. and W.D. discussed and revised parts of the manuscript. All authors have read and agreed to the published version of the manuscript.

Funding: This work was funded by the National Key Research and Development Program of China (2021YFA1501404), and the Science and Technology Commission of Shanghai Municipality (2024ZDSYS02).

Data Availability Statement: Data sharing is not applicable to this article as no new data were created or analyzed in this study.

Conflicts of Interest: The authors declare no conflicts of interest.

References

1. Fujishima, A.; Honda, K. Electrochemical photolysis of water at a semiconductor electrode. *Nature* **1972**, *238*, 37–38. [CrossRef] [PubMed]
2. Nishioka, S.; Osterloh, F.E.; Wang, X.; Mallouk, T.E.; Maeda, K. Photocatalytic water splitting. *Nat. Rev. Methods Primers* **2023**, *3*. [CrossRef]
3. Bolton, J.R.; Strickler, S.J.; Connolly, J.S. Limiting and realizable efficiencies of solar photolysis of water. *Nature* **1985**, *316*, 495–500. [CrossRef]
4. Gunawan, D.; Zhang, J.; Li, Q.; Toe, C.Y.; Scott, J.; Antonietti, M.; Guo, J.; Amal, R. Materials advances in photocatalytic solar hydrogen production: Integrating systems and economics for a sustainable future. *Adv. Mater.* **2024**, *36*, 2404618. [CrossRef] [PubMed]
5. Pinaud, B.A.; Benck, J.D.; Seitz, L.C.; Forman, A.J.; Chen, Z.; Deutsch, T.G.; James, B.D.; Baum, K.N.; Baum, G.N.; Ardo, S.; et al. Technical and economic feasibility of centralized facilities for solar hydrogen production via photocatalysis and photoelectrochemistry. *Energy Environ. Sci.* **2013**, *6*, 1983–2002. [CrossRef]
6. Wang, J.; Liao, W.; Tan, Y.; Henrotte, O.; Kang, Y.; Liu, K.; Fu, J.; Lin, Z.; Chai, L.; Cortés, E.; et al. Transfer dynamics of photo-generated carriers in catalysis. *Chem. Soc. Rev.* **2025**, *54*, 6553–6596. [CrossRef] [PubMed]
7. Yanagi, R.; Zhao, T.; Solanki, D.; Pan, Z.; Hu, S. Charge separation in photocatalysts: Mechanisms, physical parameters, and design principles. *ACS Energy Lett.* **2022**, *7*, 432–452. [CrossRef]
8. Kranz, C.; Wächtler, M. Characterizing photocatalysts for water splitting: From atoms to bulk and from slow to ultrafast processes. *Chem. Soc. Rev.* **2021**, *50*, 1407–1437. [CrossRef] [PubMed]
9. Tao, X.; Zhao, Y.; Wang, S.; Li, C.; Li, R. Recent advances and perspectives for solar-driven water splitting using particulate photocatalysts. *Chem. Soc. Rev.* **2022**, *51*, 3561–3608. [CrossRef] [PubMed]
10. Zhao, W.; Chen, H.; Zhang, J.; Low, P.J.; Sun, H. Photocatalytic overall water splitting endowed by modulation of internal and external energy fields. *Chem. Sci.* **2024**, *15*, 17292–17327. [CrossRef] [PubMed]
11. He, S.; Chen, Y.; Fang, J.; Liu, Y.; Lin, Z. Optimizing photocatalysis via electron spin control. *Chem. Soc. Rev.* **2025**, *54*, 2154–2187. [CrossRef] [PubMed]
12. Wang, Q.; Domen, K. Particulate photocatalysts for light-driven water splitting: Mechanisms, challenges, and design strategies. *Chem. Rev.* **2020**, *120*, 919–985. [CrossRef] [PubMed]
13. Mishra, B.P.; Dahiya, J.; Krishnan, V. Semiconductor photocatalysts for hydrogen evolution: Critical role of cocatalysts in enhancing performance. *Chem. Commun.* **2025**, *61*, 17302–17329. [CrossRef] [PubMed]
14. Takata, T.; Jiang, J.; Sakata, Y.; Nakabayashi, M.; Shibata, N.; Nandal, V.; Seki, K.; Hisatomi, T.; Domen, K. Photocatalytic water splitting with a quantum efficiency of almost unity. *Nature* **2020**, *581*, 411–414. [CrossRef] [PubMed]
15. Wang, Q.; Hisatomi, T.; Jia, Q.; Tokudome, H.; Zhong, M.; Wang, C.; Pan, Z.; Takata, T.; Nakabayashi, M.; Shibata, N.; et al. Scalable water splitting on particulate photocatalyst sheets with a solar-to-hydrogen energy conversion efficiency exceeding 1%. *Nat. Mater.* **2016**, *15*, 611–615. [CrossRef] [PubMed]
16. Wang, Q.; Nakabayashi, M.; Hisatomi, T.; Sun, S.; Akiyama, S.; Wang, Z.; Pan, Z.; Xiao, X.; Watanabe, T.; Yamada, T.; et al. Oxysulfide photocatalyst for visible-light-driven overall water splitting. *Nat. Mater.* **2019**, *18*, 827–832. [CrossRef] [PubMed]

17. Oshima, T.; Nishioka, S.; Kikuchi, Y.; Hirai, S.; Yanagisawa, K.-I.; Eguchi, M.; Miseki, Y.; Yokoi, T.; Yui, T.; Kimoto, K.; et al. An artificial Z-scheme constructed from dye-sensitized metal oxide nanosheets for visible light-driven overall water splitting. *J. Am. Chem. Soc.* **2020**, *142*, 8412–8420. [CrossRef] [PubMed]
18. Nishiyama, H.; Yamada, T.; Nakabayashi, M.; Maehara, Y.; Yamaguchi, M.; Kuromiya, Y.; Nagatsuma, Y.; Tokudome, H.; Akiyama, S.; Watanabe, T.; et al. Photocatalytic solar hydrogen production from water on a 100-m^2 scale. *Nature* **2021**, *598*, 304–307. [CrossRef] [PubMed]
19. Yang, J.H.; Wang, D.; Han, H.X.; Li, C. Roles of cocatalysts in photocatalysis and photoelectrocatalysis. *Acc. Chem. Res.* **2013**, *46*, 1900–1909. [CrossRef] [PubMed]
20. Zhao, H.; Mao, Q.; Jian, L.; Dong, Y.; Zhu, Y. Photodeposition of earth-abundant cocatalysts in photocatalytic water splitting: Methods, functions, and mechanisms. *Chin. J. Catal.* **2022**, *43*, 1774–1804. [CrossRef]
21. Chen, Y.; Agrelo-Lestón, A.; Burgués-Ceballos, I.; Llorca, J.; Soler, L. Bimetallic nanoparticles as cocatalysts for photocatalytic hydrogen production. *Adv. Funct. Mater.* **2026**, *36*, e06279. [CrossRef]
22. Wu, C.; Lv, K.; Li, X.; Li, Q. Dual cocatalysts for photocatalytic hydrogen evolution: Categories, synthesis, and design considerations. *Chin. J. Catal.* **2023**, *54*, 137–160. [CrossRef]
23. Hinnemann, B.; Moses, P.G.; Bonde, J.; Jørgensen, K.P.; Nielsen, J.H.; Horch, S.; Chorkendorff, I.; Nørskov, J.K. Biomimetic hydrogen evolution: MoS2 nanoparticles as catalyst for hydrogen evolution. *J. Am. Chem. Soc.* **2005**, *127*, 5308–5309. [CrossRef] [PubMed]
24. Zong, X.; Yan, H.J.; Wu, G.P.; Ma, G.; Wen, F.; Wang, L.; Li, C. Enhancement of photocatalytic H_2 evolution on CdS by loading MoS_2 as cocatalyst under visible-light irradiation. *J. Am. Chem. Soc.* **2008**, *130*, 7176–7177. [CrossRef] [PubMed]
25. Yan, H.; Yang, J.; Ma, G.; Wu, G.; Zong, X.; Lei, Z.; Shi, J.; Li, C. Visible-light-driven hydrogen production with extremely high quantum efficiency on Pt-PdS/CdS photocatalyst. *J. Catal.* **2009**, *266*, 165–168. [CrossRef]
26. Yang, J.; Yan, H.; Wang, X.; Wen, F.; Wang, Z.; Fan, D.; Shi, J.; Li, C. Roles of cocatalysts in Pt-PdS/CdS with exceptionally high quantum efficiency for photocatalytic hydrogen production. *J. Catal.* **2012**, *290*, 151–157. [CrossRef]
27. Wang, D.; Li, R.; Zhu, J.; Shi, J.; Han, J.; Zong, X.; Li, C. Photocatalytic water oxidation on $BiVO_4$ with the electrocatalyst as an oxidation cocatalyst: Essential relations between electrocatalyst and photocatalyst. *J. Phys. Chem. C* **2012**, *116*, 5082–5089. [CrossRef]
28. Zhong, D.K.; Choi, S.; Gamelin, D.R. Near-complete suppression of surface recombination in solar photoelectrolysis by Co-Pi catalyst-modified W:$BiVO_4$. *J. Am. Chem. Soc.* **2011**, *133*, 18370–18377. [CrossRef] [PubMed]
29. Maeda, K.; Xiong, A.; Yoshinaga, T.; Ikeda, T.; Sakamoto, N.; Hisatomi, T.; Takashima, M.; Lu, D.; Kanehara, M.; Setoyama, T.; et al. Photocatalytic overall water splitting promoted by two different cocatalysts for hydrogen and oxygen evolution under visible light. *Angew. Chem. Int. Ed.* **2010**, *49*, 4096–4099. [CrossRef] [PubMed]
30. Murali, G.; Modigunta, J.K.R.; Park, Y.H.; Lee, J.-H.; Rawal, J.; Lee, S.-Y.; In, I.; Park, S.-J. A review on MXene synthesis, stability, and photocatalytic applications. *ACS Nano* **2022**, *16*, 13370–13429. [CrossRef] [PubMed]
31. Miao, B.; Bashir, T.; Zhang, H.; Ali, T.; Raza, S.; He, D.; Liu, Y.; Bai, J. Impact of various 2D MXene surface terminating groups in energy conversion. *Renew. Sustain. Energy Rev.* **2024**, *199*, 114506. [CrossRef]
32. Thangavelu, H.H.S.; Huang, C.; Chabanais, F.; Palisaitis, J.; Persson, P.O.Å. A review on MXene terminations. *Adv. Funct. Mater.* **2026**, *36*, e15604. [CrossRef]
33. Liao, J.; Pang, S.-Y.; Hao, J. Multi-scale interface engineering of MXenes for multifunctional sensory systems. *Adv. Funct. Mater.* **2026**, *36*, e00047. [CrossRef]
34. Naguib, M.; Kurtoglu, M.; Presser, V.; Lu, J.; Niu, J.; Heon, M.; Hultman, L.; Gogotsi, Y.; Barsoum, M.W. Two-dimensional nanocrystals produced by exfoliation of Ti_3AlC_2. *Adv. Mater.* **2011**, *23*, 4248–4253. [CrossRef] [PubMed]
35. Ghidiu, M.; Lukatskaya, M.R.; Zhao, M.-Q.; Gogotsi, Y.; Barsoum, M.W. Conductive two-dimensional titanium carbide "clay" with high volumetric capacitance. *Nature* **2014**, *516*, 78–81. [CrossRef] [PubMed]
36. Lipatov, A.; Alhabeb, M.; Lukatskaya, M.R.; Boson, A.J.; Gogotsi, Y.; Sinitskii, A. Effect of synthesis on quality, electronic properties and environmental stability of individual monolayer Ti_3C_2 MXene flakes. *Adv. Electron. Mater.* **2016**, *2*, 1600255. [CrossRef]
37. Khazaei, M.; Arai, M.; Sasaki, T.; Chung, C.-Y.; Venkataramanan, N.S.; Estili, M.; Sakka, Y.; Kawazoe, Y. Novel electronic and magnetic properties of two-dimensional transition metal carbides and nitrides. *Adv. Funct. Mater.* **2013**, *23*, 2185–2192. [CrossRef]
38. Li, M.; Lu, J.; Luo, K.; Li, Y.; Chang, K.; Chen, K.; Zhou, J.; Rosen, J.; Hultman, L.; Eklund, P.; et al. Element replacement approach by reaction with Lewis acidic molten salts to synthesize nanolaminated MAX phases and MXenes. *J. Am. Chem. Soc.* **2019**, *141*, 4730–4737. [CrossRef] [PubMed]
39. Li, Y.; Shao, H.; Lin, Z.; Lu, J.; Liu, L.; Duployer, B.; Persson, P.O.Å.; Eklund, P.; Hultman, L.; Li, M.; et al. A general Lewis acidic etching route for preparing MXenes with enhanced electrochemical performance in non-aqueous electrolyte. *Nat. Mater.* **2020**, *19*, 894–899. [CrossRef] [PubMed]
40. Kamysbayev, V.; Filatov, A.S.; Hu, H.; Rui, X.; Lagunas, F.; Wang, D.; Klie, R.F.; Talapin, D.V. Covalent surface modifications and superconductivity of two-dimensional metal carbide MXenes. *Science* **2020**, *369*, 979–983. [CrossRef] [PubMed]

41. Khazaei, M.; Arai, M.; Sasaki, T.; Ranjbar, A.; Liang, Y.; Yunoki, S. OH-terminated two-dimensional transition metal carbides and nitrides as ultralow work function materials. *Phys. Rev. B* **2015**, *92*, 075411. [CrossRef]
42. Liu, Y.; Xiao, H.; Goddard, W.A., III. Schottky-barrier-free contacts with two-dimensional semiconductors by surface-engineered MXenes. *J. Am. Chem. Soc.* **2016**, *138*, 15853–15856. [CrossRef] [PubMed]
43. Ran, J.; Gao, G.; Li, F.-T.; Ma, T.-Y.; Du, A.; Qiao, S.-Z. Ti_3C_2 MXene co-catalyst on metal sulfide photo-absorbers for enhanced visible-light photocatalytic hydrogen production. *Nat. Commun.* **2017**, *8*, 13907. [CrossRef] [PubMed]
44. Peng, C.; Wei, P.; Li, X.; Liu, Y.; Cao, Y.; Wang, H.; Yu, H.; Peng, F.; Zhang, L.; Zhang, B.; et al. High efficiency photocatalytic hydrogen production over ternary $Cu/TiO_2@Ti_3C_2T_x$ enabled by low-work-function 2D titanium carbide. *Nano Energy* **2018**, *53*, 97–107. [CrossRef]
45. Xie, X.; Zhang, N. Positioning MXenes in the photocatalysis landscape: Competitiveness, challenges, and future perspectives. *Adv. Funct. Mater.* **2020**, *30*, 2002528. [CrossRef]
46. Lee, D.E.; Danish, M.; Jo, W.K. A review of the interfacial chemistry of Ti_3C_2 MXene-coordinated nanocomposites for photocatalytic green H_2 evolution. *Coord. Chem. Rev.* **2024**, *517*, 216022. [CrossRef]
47. Pugazhendhi, A.; Kamarudin, S.K.; Brindhadevi, K. MXenes as catalyst for sustainable hydrogen production. *Renew. Sustain. Energy Rev.* **2026**, *226*, 116376. [CrossRef]
48. Tang, Q.; Li, T.; Tu, W.; Wang, H.; Zhou, Y.; Zou, Z. Recent advances in diverse MXenes-based structures for photocatalytic CO_2 reduction into renewable hydrocarbon fuels. *Adv. Funct. Mater.* **2024**, *34*, 2311609. [CrossRef]
49. Gul, I.; Sayed, M.; Saeed, T.; Rehman, F.; Naeem, A.; Gul, S.; Khan, Q.; Naz, K.; ur Rehman, M. Unveiling cutting-edge progress in the fundamentals of MXene: Synthesis strategies, energy and bio-environmental applications. *Coord. Chem. Rev.* **2024**, *511*, 215870. [CrossRef]
50. Wang, H.; Peng, R.; Hood, Z.D.; Naguib, M.; Adhikari, S.P.; Wu, Z. Titania composites with 2D transition metal carbides as photocatalysts for hydrogen production under visible-light irradiation. *ChemSusChem* **2016**, *9*, 1490–1497. [CrossRef] [PubMed]
51. Xiao, R.; Zhao, C.; Zou, Z.; Chen, Z.; Tian, L.; Xu, H.; Tang, H.; Liu, Q.; Lin, Z.; Yang, X. In situ fabrication of 1D CdS nanorod/2D Ti_3C_2 MXene nanosheet Schottky heterojunction toward enhanced photocatalytic hydrogen evolution. *Appl. Catal. B Environ.* **2020**, *268*, 118382. [CrossRef]
52. Cao, S.; Shen, B.; Tong, T.; Fu, J.; Yu, J. 2D/2D heterojunction of ultrathin MXene/Bi_2WO_6 nanosheets for improved photocatalytic CO_2 reduction. *Adv. Funct. Mater.* **2018**, *28*, 1800136. [CrossRef]
53. Peng, C.; Yang, X.; Li, Y.; Yu, H.; Wang, H.; Peng, F. Hybrids of two-dimensional Ti_3C_2 and TiO_2 exposing {001} facets toward enhanced photocatalytic activity. *ACS Appl. Mater. Interfaces* **2016**, *8*, 6051–6060. [CrossRef] [PubMed]
54. Su, T.; Men, C.; Chen, L.; Chu, B.; Luo, X.; Ji, H.; Chen, J.; Qin, Z. Sulfur vacancy and $Ti_3C_2T_x$ cocatalyst synergistically boosting interfacial charge transfer in 2D/2D $Ti_3C_2T_x/ZnIn_2S_4$ heterostructure for enhanced photocatalytic hydrogen evolution. *Adv. Sci.* **2022**, *9*, 2103715. [CrossRef] [PubMed]
55. Cai, M.; Zha, X.; Zhuo, Z.; Bai, J.; Wang, Q.; Cheng, Q.; Wei, Y.; Sun, S. Enhanced photocatalytic hydrogen production of $ZnIn_2S_4$ by using surface-engineered $Ti_3C_2T_x$ MXene as a cocatalyst. *Materials* **2023**, *16*, 2168. [CrossRef] [PubMed]
56. Huang, T.Y.; Yang, Z.; Yang, S.Y.; Dai, Z.H.; Liu, Y.J.; Liao, J.H.; Zhong, G.Y.; Xie, Z.J.; Fang, Y.P.; Zhang, S.S. Construction of 2D/2D $Ti_3C_2T_x$ MXene/CdS heterojunction with photothermal effect for efficient photocatalytic hydrogen production. *J. Mater. Sci. Technol.* **2024**, *171*, 1–9. [CrossRef]
57. Wu, C.; Huang, W.; Liu, H.; Lv, K.; Li, Q. Insight into synergistic effect of Ti_3C_2 MXene and MoS_2 on anti-photocorrosion and photocatalytic activity of CdS for hydrogen production. *Appl. Catal. B Environ.* **2023**, *330*, 122653. [CrossRef]
58. Ding, M.; Xiao, R.; Zhao, C.; Bukhvalov, D.; Chen, Z.; Xu, H.; Tang, H.; Xu, J.; Yang, X. Evidencing interfacial charge transfer in 2D CdS/2D MXene Schottky heterojunctions toward high-efficiency photocatalytic hydrogen production. *Sol. RRL* **2021**, *5*, 2000414. [CrossRef]
59. Wei, K.; Yang, J.-X.; Bai, F.-Y.; Shen, Y.-S.; Liu, K.; Liu, J.; Chen, L.-H.; Li, Y.; Su, B.-L. In situ conversion of Ti_3C_2 MXene to sandwich Ti_3C_2/R-TiO_2 for promoted photocatalytic hydrogen production. *ACS Appl. Energy Mater.* **2023**, *6*, 5456–5463. [CrossRef]
60. Sherryna, A.; Tahir, M. Role of surface morphology and terminating groups in titanium carbide MXenes ($Ti_3C_2T_x$) cocatalysts with engineering aspects for modulating solar hydrogen production: A critical review. *Chem. Eng. J.* **2022**, *433*, 134573. [CrossRef]
61. Zhang, K.; Li, D.; Cao, H.; Zhu, Q.; Trapalis, C.; Zhu, P.; Gao, X.; Wang, C. Insights into different dimensional MXenes for photocatalysis. *Chem. Eng. J.* **2021**, *424*, 130340. [CrossRef]
62. Wang, H.; Sun, Y.; Wu, Y.; Tu, W.; Wu, S.; Yuan, X.; Zeng, G.; Xu, Z.J.; Li, S.; Chew, J.W. Electrical promotion of spatially photoinduced charge separation via interfacial-built-in quasi-alloying effect in hierarchical $Zn_2In_2S_5/Ti_3C_2(O,OH)_x$ hybrids toward efficient photocatalytic hydrogen evolution and environmental remediation. *Appl. Catal. B Environ.* **2019**, *245*, 290–301. [CrossRef]
63. Zuo, G.; Wang, Y.; Teo, W.L.; Xie, A.; Guo, Y.; Dai, Y.; Zhou, W.; Jana, D.; Xian, Q.; Dong, W.; et al. Ultrathin $ZnIn_2S_4$ nanosheets anchored on $Ti_3C_2T_x$ MXene for photocatalytic H_2 evolution. *Angew. Chem. Int. Ed.* **2020**, *59*, 11287–11292. [CrossRef] [PubMed]

64. Xu, H.; Xiao, R.; Huang, J.; Jiang, Y.; Zhao, C.; Yang, X. In situ construction of protonated g-C_3N_4/$Ti_3C_2T_x$ MXene Schottky heterojunctions for efficient photocatalytic hydrogen production. *Chin. J. Catal.* **2021**, *42*, 107–114. [CrossRef]
65. Li, Y.; Liu, Y.; Wang, Z.; Wang, P.; Zheng, Z.; Cheng, H.; Dai, Y.; Huang, B. In-situ growth of Ti_3C_2@MIL-NH_2 composite for highly enhanced photocatalytic H_2 evolution. *Chem. Eng. J.* **2021**, *411*, 128446. [CrossRef]
66. Liu, Y.; Li, Y.-H.; Li, X.; Zhang, Q.; Yu, H.; Peng, X.; Peng, F. Regulating electron–hole separation to promote photocatalytic H_2 evolution activity of nanoconfined Ru/MXene/TiO_2 catalysts. *ACS Nano* **2020**, *14*, 14181–14189. [CrossRef] [PubMed]
67. Sun, Y.; Jin, D.; Sun, Y.; Meng, X.; Gao, Y.; Dall'Agnese, Y.; Chen, G.; Wang, X.-F. g-C_3N_4/$Ti_3C_2T_x$ (MXenes) composite with oxidized surface groups for efficient photocatalytic hydrogen evolution. *J. Mater. Chem. A* **2018**, *6*, 9124–9131. [CrossRef]
68. Su, T.; Hood, Z.D.; Naguib, M.; Bai, L.; Luo, S.; Rouleau, C.M.; Ivanov, I.N.; Ji, H.; Qin, Z.; Wu, Z. 2D/2D heterojunction of Ti_3C_2/g-C_3N_4 nanosheets for enhanced photocatalytic hydrogen evolution. *Nanoscale* **2019**, *11*, 8138–8149. [CrossRef] [PubMed]
69. Chen, X.; Guo, Y.; Bian, R.; Ji, Y.; Wang, X.; Zhang, X.; Cui, H.; Tian, J. Titanium carbide MXenes coupled with cadmium sulfide nanosheets as two-dimensional/two-dimensional heterostructures for photocatalytic hydrogen production. *J. Colloid Interface Sci.* **2022**, *613*, 644–651. [CrossRef] [PubMed]
70. Yang, Y.; Zhang, D.; Xiang, Q. Plasma-modified $Ti_3C_2T_x$/CdS hybrids with oxygen-containing groups for high-efficiency photocatalytic hydrogen production. *Nanoscale* **2019**, *11*, 18797–18805. [CrossRef] [PubMed]
71. Huang, W.; Li, Z.; Wu, C.; Zhang, H.; Sun, J.; Li, Q. Delaminating Ti_3C_2 MXene by blossom of $ZnIn_2S_4$ microflowers for noble-metal-free photocatalytic hydrogen production. *J. Mater. Sci. Technol.* **2022**, *120*, 89–98. [CrossRef]
72. Liu, P.; Zhao, Y.; Liu, W.; Ye, F.; Lv, H.; Peng, Z.; Han, C.; Ma, X.; Tian, J.; Zhan, D.; et al. In situ oxidative growth to form compact TiO_2-Ti_3C_2 heterojunctions for photocatalytic hydrogen evolution. *Int. J. Hydrogen Energy* **2024**, *80*, 1243–1254, Retraction in *Int. J. Hydrogen Energy* 2026, *in press*. [CrossRef]
73. Zhang, Y.; Zhang, Z.; Li, Q.; Gao, X.; Lu, Q.; Guo, E.; Si, C.; Wei, M. Zero-dimensional/two-dimensional Schottky junction of $Mn_{0.5}Cd_{0.5}S$/Ti_3C_2 MXene induces rapid electron transfer and enrichment for boosting photocatalytic H_2 production activity. *Energy Fuels* **2024**, *38*, 5457–5464. [CrossRef]
74. Liu, S.J.; Fang, H.X.; Chen, R.; Ma, Y.; Zhu, Y.; Ye, M.; Zhang, H.; Zhang, K. Bridging CdS with $Ti_3C_2T_x$ nanosheets via ligands for enhanced charge transfer in photocatalytic H_2 production. *Int. J. Hydrogen Energy* **2024**, *54*, 1154–1159. [CrossRef]
75. Kalita, S.J.; Varangane, S.; Basyach, P.; Sonowal, K.; Abraham, B.M.; Guha, A.K.; Pal, U.; Saikia, L. $InVO_4$-decorated Ti_3C_2 MXene for efficient photocatalytic hydrogen evolution. *ACS Appl. Mater. Interfaces* **2024**, *16*, 40825–40835. [CrossRef] [PubMed]
76. Yang, J.; Wang, R.; Sun, X.R.; Li, Y.; Liu, J.; Kuang, X. Au/Ti_3C_2/g-C_3N_4 ternary composites boost H_2 evolution efficiently with remarkable long-term stability by synergistic strategies. *ACS Appl. Mater. Interfaces* **2024**, *16*, 12385–12397. [CrossRef] [PubMed]
77. Herber, M.; Hill, E.H. Templated growth of In2S3 in $Ti_3C_2T_x$ MXene with enhanced photocatalytic properties. *Sol. RRL* **2024**, *8*, 2400282. [CrossRef]
78. Hu, Q.Q.; Yin, H.Y.; Liu, Y.F.; Ablez, A.; Wang, Z.; Zhan, Y.; Du, C.; Huang, X. Tailoring the morphology and charge-transfer pathways of ultrathin $Cd_{0.8}Zn_{0.2}S$ nanosheets via ionic-liquid-modified Ti_3C_2 MXenes toward remarkable photocatalytic hydrogen evolution. *J. Mater. Sci. Technol.* **2025**, *204*, 47–59. [CrossRef]
79. Changotra, R.; Yang, J.; Dasog, M.; He, Q.S. Schottky-driven interfacial design of Bi_2MoO_6/$Ti_3C_2T_x$ heterostructure for boosted piezocatalytic hydrogen evolution. *Commun. Mater.* **2026**, *7*, 181. [CrossRef] [PubMed]
80. Liu, Q.; Han, X.; Qian, A.; Qian, J.; Pu, X.; Ye, L.; Zhan, J.; Zhang, J.; Yang, Q.; Liu, J. Heterostructuring uniform 2D CdS on Ru/Ti_3C_2-TiO_2 via in situ oxidized Ru-loaded MXene for boosting photocatalytic H_2 production. *Small* **2025**, *21*, 2407399. [CrossRef] [PubMed]
81. Bao, J.; Zhang, X.; Xiao, W.; Yuan, H.; Huang, B.; He, G. Design of 3D/1D/2D $ZnIn_2S_4$/$Zn_{0.2}Cd_{0.8}S$/Ti_3C_2 MXene interfacial heterojunction for enhanced photocatalytic hydrogen evolution. *Surf. Interfaces* **2025**, *56*, 105644. [CrossRef]
82. Ren, M.; Li, J.; Guo, D.; Zhang, D.; Zhuang, Y.; Meng, S.; Li, X.; Yang, X.; Sui, G. Lattice coherency engineering triggers rapid charge transport at the heterointerface of Te/In_2O_3@MXene photocatalysts for boosting photocatalytic hydrogen evolution. *J. Colloid Interface Sci.* **2025**, *685*, 733–742. [CrossRef] [PubMed]
83. Liao, Y.; Wang, X.; Gu, H.; Zhang, H.; Meng, J.; Dai, W.-L. Synthesis and recent developments of MXene-based composites for photocatalytic hydrogen production. *J. Phys. D Appl. Phys.* **2024**, *57*, 482001. [CrossRef]
84. Gu, H.; Zhang, H.; Wang, X.; Li, Q.; Chang, S.; Huang, Y.; Gao, L.; Cui, Y.; Liu, R.; Dai, W.-L. Robust construction of CdSe nanorods@Ti_3C_2 MXene nanosheet for superior photocatalytic H_2 evolution. *Appl. Catal. B Environ.* **2023**, *328*, 122537. [CrossRef]
85. Li, Q.; Zhang, H.; Gu, H.; Cui, Y.; Gao, R.; Dai, W.-L. In situ growth of $Cd_{0.5}Zn_{0.5}S$ nanorods on Ti_3C_2 MXene nanosheet for efficient visible-light-driven photocatalytic hydrogen evolution. *Acta Phys.-Chim. Sin.* **2025**, *41*, 100031. [CrossRef]
86. Li, Y.; Zhang, Y.; Hou, R.; Ai, Y.; Cai, M.; Shi, Z.; Zhang, P.; Shao, G. Revealing electron numbers–binding energy relationships in heterojunctions via in-situ irradiated XPS. *Appl. Catal. B Environ. Energy* **2024**, *356*, 124223. [CrossRef]
87. Xing, W.; Lin, H.; Shao, W.; Jian, N.; Liu, T.; Wen, S.; Han, J.; Wu, G. Heteroatom- and bonded-tailored Schottky barrier in Ti_3C_2 MXene/carbon nitride heterojunctions toward efficient photocatalysis. *Chem. Eng. J.* **2025**, *520*, 166126. [CrossRef]

88. Näslund, L.Å.; Kokkonen, E.; Magnuson, M. Interaction and kinetics of H_2, CO_2, and H_2O on $Ti_3C_2T_x$ MXene probed by X-ray photoelectron spectroscopy. *Appl. Surf. Sci.* **2025**, *684*, 161926. [CrossRef]
89. Yu, P.; Chen, S.; Wang, Y.; Li, J.; Zhang, Z.; Zhao, S.; Zhang, Y.; Zhou, Y. 3D/2D coral-like C_3N_5/Ti_3C_2 MXene Schottky heterojunction for enhanced photocatalytic H_2 evolution. *Int. J. Hydrogen Energy* **2024**, *58*, 1266–1276. [CrossRef]
90. Zhang, Y.; Zhou, K.; Yuan, C.; Lv, H.; Yin, H.; Fei, Q.; Xiao, D.; Zhang, Y.; Lau, W. In-situ formation of $SrTiO_3/Ti_3C_2$ MXene Schottky heterojunction for efficient photocatalytic hydrogen evolution. *J. Colloid Interface Sci.* **2024**, *653*, 482–492. [CrossRef] [PubMed]
91. Wu, H.; Lou, Z.; Kang, K.; Zhang, C.; Ji, X.; Chu, H.; Wei, S.; Xu, W.; Wang, G.; Pan, J.; et al. Constructed 2D sandwich-like layer $WO_3/Ti_3C_2/ZnIn_2S_4$ Z-scheme heterojunction by chemical bond for effective photocatalytic hydrogen production. *J. Colloid Interface Sci.* **2025**, *682*, 403–412. [CrossRef] [PubMed]
92. Li, R.; Li, H.; Li, H.; Zhang, X.; Zhao, Y.; Feng, K.; Sun, W.; Zhou, Y.; Yu, J.; Liu, G.; et al. Orchestrating single Ru atoms and second-shell cation vacancies in CdS interfaced with $Ti_3C_2T_x$ MXene for boosting photocatalytic hydrogen evolution. *Adv. Funct. Mater.* **2026**, *36*, e74535. [CrossRef]
93. Tian, L.; Xu, F.; Sastre, G.; Primo, A.; Yu, J.; García, H. Engineering MXene surfaces and heterostructure interfaces for efficient heterogeneous catalysis. *Chem. Soc. Rev.* **2026**, *55*, 4244–4302. [CrossRef] [PubMed]
94. Zhang, J.; Zhao, Y.; Guo, X.; Chen, C.; Dong, C.-L.; Liu, R.-S.; Han, C.-P.; Li, Y.; Gogotsi, Y.; Wang, G. Single platinum atoms immobilized on an MXene as an efficient catalyst for the hydrogen evolution reaction. *Nat. Catal.* **2018**, *1*, 985–992. [CrossRef]
95. Zhang, H.; Huang, Y.; Wang, X.; Meng, J.; Gao, L.; Li, Y.; Zhang, Y.; Liao, Y.; Dai, W.-L. Tightly-bound interfaces between $ZnIn_2S_4$ nanosheets and few-layered Mo_2TiC_2 MXene induced highly efficient noble-metal-free Schottky junction for photocatalytic hydrogen evolution. *Sep. Purif. Technol.* **2025**, *360*, 131199. [CrossRef]
96. Fan, Y.; Hao, X.; Yi, N.; Jin, Z. Strong electronic coupling of Mo_2TiC_2 MXene/ZnCdS ohmic junction for boosting photocatalytic hydrogen evolution. *Appl. Catal. B Environ. Energy* **2024**, *357*, 124313. [CrossRef]
97. Li, B.; Li, T.; Ma, X.; Lei, M.; Jin, Z.; Tsubaki, N.; Fornasiero, P. Boosting charge separation in a $CdIn_2S_4/Mo_2TiC_2$ MXene Schottky heterojunction for enhanced photocatalytic hydrogen production. *EcoEnergy* **2026**, *4*, e70045. [CrossRef]
98. Ding, L.; Zeng, S.; Zhang, W.; Guo, C.; Chen, X.; Peng, B.; Lv, Z.-P.; Zhou, H.; Xu, Q. Nitrogen-doped Ti_3C_2 MXene quantum dots/1D CdS nanorod heterostructure photocatalyst of highly efficient hydrogen evolution. *ACS Appl. Energy Mater.* **2022**, *5*, 11540–11552. [CrossRef]
99. Li, J.; Peng, H.; Luo, B.; Cao, J.; Ma, L.; Jing, D. The enhanced photocatalytic and photothermal effects of Ti_3C_2 MXene quantum dot/macroscopic porous graphitic carbon nitride heterojunction for hydrogen production. *J. Colloid Interface Sci.* **2023**, *641*, 309–318. [CrossRef] [PubMed]
100. Wang, L.; Yang, T.; Peng, L.; Zhang, Q.; She, X.; Tang, H.; Liu, Q. Dual transfer channels of photo-carriers in 2D/2D/2D sandwich-like $ZnIn_2S_4$/g-C_3N_4/Ti_3C_2 MXene S-scheme/Schottky heterojunction for boosting photocatalytic H_2 evolution. *Chin. J. Catal.* **2022**, *43*, 2720–2731. [CrossRef]
101. Hart, J.L.; Hantanasirisakul, K.; Lang, A.C.; Anasori, B.; Pinto, D.; Pivak, Y.; van Omme, J.T.; May, S.J.; Gogotsi, Y.; Taheri, M.L. Control of MXenes' electronic properties through termination and intercalation. *Nat. Commun.* **2019**, *10*, 522. [CrossRef] [PubMed]
102. Rems, E.; Hu, Y.-J.; Gogotsi, Y.; Dominko, R. Pivotal role of surface terminations in MXene thermodynamic stability. *Chem. Mater.* **2024**, *36*, 10295–10306. [CrossRef] [PubMed]
103. Li, D.; Zheng, W.; Ghorbani-Asl, M.; Scheiter, J.; Sobczak, K.; Kretschmer, S.; Polčák, J.; Jadhao, P.H.; Michałowski, P.P.; Yu, R.; et al. Triphasic synthesis of MXenes with uniform and controlled halogen terminations. *Nat. Synth.* **2026**, *5*, 516–526. [CrossRef]
104. Cheng, Y.-W.; Dai, J.-H.; Zhang, Y.-M.; Song, Y. Two-dimensional, ordered, double transition metal carbides (MXenes): A new family of promising catalysts for the hydrogen evolution reaction. *J. Phys. Chem. C* **2018**, *122*, 28113–28122. [CrossRef]
105. Luxa, J.; Kupka, P.; Lipilin, F.; Šturala, J.; Subramani, A.; Lazar, P.; Sofer, Z. Hydrogen evolution reaction activity in $Mo_2TiC_2T_x$ MXene derived from Mo_2TiAlC_2 MAX phase: Insights from compositional transformations. *ACS Catal.* **2024**, *14*, 15336–15347. [CrossRef] [PubMed]
106. Du, J.; Yan, Y.; Li, X.; Chen, J.; Guo, C.; Chen, Y.; Wang, H. A mechanism-guided descriptor for the hydrogen evolution reaction in 2D ordered double transition-metal carbide MXenes. *Chem. Sci.* **2025**, *16*, 9424–9435. [CrossRef] [PubMed]
107. Jin, D.; Johnson, L.R.; Raman, A.S.; Ming, X.; Gao, Y.; Du, F.; Wei, Y.; Chen, G.; Vojvodic, A.; Gogotsi, Y.; et al. Computational screening of 2D ordered double transition-metal carbides (MXenes) as electrocatalysts for hydrogen evolution reaction. *J. Phys. Chem. C* **2020**, *124*, 10584–10592. [CrossRef]
108. Zeng, Z.; Chen, X.; Weng, K.; Wu, Y.; Zhang, P.; Jiang, J.; Li, N. Computational screening study of double transition metal carbonitrides $M'_2M''CNO_2$-MXene as catalysts for hydrogen evolution reaction. *npj Comput. Mater.* **2021**, *7*, 80. [CrossRef]
109. Wang, X.; Wang, C.; Ci, S.; Ma, Y.; Liu, T.; Gao, L.; Qian, P.; Ji, C.; Su, Y. Accelerating 2D MXene catalyst discovery for the hydrogen evolution reaction by computer-driven workflow and an ensemble learning strategy. *J. Mater. Chem. A* **2020**, *8*, 23488–23497. [CrossRef]

110. Hantanasirisakul, K.; Alhabeb, M.; Lipatov, A.; Maleski, K.; Anasori, B.; Salles, P.; Ieosakulrat, C.; Pakawatpanurut, P.; Sinitskii, A.; May, S.J.; et al. Effects of synthesis and processing on optoelectronic properties of titanium carbonitride MXene. *Chem. Mater.* **2019**, *31*, 2941–2951. [CrossRef]
111. Wang, D.; Zhou, C.; Filatov, A.S.; Cho, W.; Lagunas, F.; Wang, M.; Vaikuntanathan, S.; Liu, C.; Klie, R.F.; Talapin, D.V. Direct synthesis and chemical vapor deposition of 2D carbide and nitride MXenes. *Science* **2023**, *379*, 1242–1247. [CrossRef] [PubMed]
112. Ling, C.; Shi, L.; Ouyang, Y.; Wang, J. Searching for highly active catalysts for hydrogen evolution reaction based on O-terminated MXenes through a simple descriptor. *Chem. Mater.* **2016**, *28*, 9026–9032. [CrossRef]
113. Pandey, M.; Thygesen, K.S. Two-dimensional MXenes as catalysts for electrochemical hydrogen evolution: A computational screening study. *J. Phys. Chem. C* **2017**, *121*, 13593–13598. [CrossRef]
114. Tiwari, A.P.; McBride, S.; Hamlin, A.B.; Rahman, M.S.; Huddy, J.E.; Hautier, G.; Scheideler, W.J. MXene anion engineering for efficient hydrogen evolution. *ACS Sustain. Chem. Eng.* **2023**, *11*, 12084–12092. [CrossRef]
115. Li, H.; Chen, Y.; Tang, Q. Surface termination (−O, −F or −OH) and metal doping on the HER activity of Mo_2CT_x MXene. *ChemPhysChem* **2024**, *25*, e202400255. [CrossRef] [PubMed]
116. Kumari, A.; Singh, S.; Munde, R.; Bashir, A.U.; Ingole, P.P.; Ghosh, D. Hydrogen evolution on halogenated MXenes via surface termination engineering: A data-informed computational and experimental strategy. *J. Mater. Chem. A* **2025**, *13*, 42410–42426. [CrossRef]
117. Kuznetsov, D.A.; Chen, Z.; Kumar, P.V.; Tsoukalou, A.; Kierzkowska, A.; Abdala, P.M.; Safonova, O.V.; Fedorov, A.; Müller, C.R. Single site cobalt substitution in 2D molybdenum carbide (MXene) enhances catalytic activity in the hydrogen evolution reaction. *J. Am. Chem. Soc.* **2019**, *141*, 17809–17816. [CrossRef] [PubMed]
118. Wyatt, B.C.; Thakur, A.; Nykiel, K.; Hood, Z.D.; Adhikari, S.P.; Pulley, K.K.; Highland, W.J.; Strachan, A.; Anasori, B. Design of atomic ordering in $Mo_2Nb_2C_3T_x$ MXenes for hydrogen evolution electrocatalysis. *Nano Lett.* **2023**, *23*, 931–938. [CrossRef] [PubMed]
119. Ramalingam, V.; Varadhan, P.; Fu, H.-C.; Kim, H.; Zhang, D.; Chen, S.; Song, L.; Ma, D.; Wang, Y.; Alshareef, H.N.; et al. Heteroatom-mediated interactions between ruthenium single atoms and an MXene support for efficient hydrogen evolution. *Adv. Mater.* **2019**, *31*, 1903841. [CrossRef] [PubMed]
120. Wu, Y.; Wang, L.; Bo, T.; Chai, Z.; Gibson, J.K.; Shi, W. Boosting hydrogen evolution in neutral medium by accelerating water dissociation with Ru clusters loaded on Mo_2CT_x MXene. *Adv. Funct. Mater.* **2023**, *33*, 2214375. [CrossRef]
121. Sun, Y.; Lee, J.; Kwon, N.H.; Lim, J.; Jin, X.; Gogotsi, Y.; Hwang, S.-J. Enhancing hydrogen evolution reaction activity of palladium catalyst by immobilization on MXene nanosheets. *ACS Nano* **2024**, *18*, 6243–6255. [CrossRef] [PubMed]
122. Wang, F.; Jin, S.; Du, Y.; Xia, Q.; Wang, L.; Zhou, A. Preparation of Mo_2CT_x MXene as co-catalyst for H_2 production by etching of pure/mixed HBr solution. *Diam. Relat. Mater.* **2023**, *136*, 109922. [CrossRef]
123. Huang, W.-H.; Huang, B.-H.; Hsiao, P.-K.; Pu, Y.-C.; Chen, I.-W.P. Visible light-responsive bimetallic Mo_2TiC_2 MXenes for enhanced hydrogen evolution performance. *J. Phys. Chem. C* **2026**, *130*, 5733–5740. [CrossRef]
124. Xi, Q.; Liu, J.; Xie, F.; Jian, A.; Sun, Z.; Zhou, A.; Jian, X.; Zhang, X.; Wang, Y.; Li, H.; et al. Electron-parking engineering assisted $ZnIn_2S_4/Mo_2TiC_2$-Ru photocatalytic hydrogen evolution for efficient solar energy conversion and storage. *Appl. Catal. B Environ. Energy* **2024**, *355*, 124184. [CrossRef]
125. Yin, H.; Du, J.; Ma, X.; Li, Y.; Jin, Z. Efficient photocatalytic hydrogen production through $Mn_{0.4}Cd_{0.6}S$/2D Mo_2TiC_2 MXene ohmic junction with effective light corrosion resistance. *Adv. Sustain. Syst.* **2026**, *10*, e01465. [CrossRef]
126. Du, J.; Yang, H.; Jin, F.; Jiang, G.; Jin, Z. Engineering strong electronic coupling on Mo_2TiC_2 MXene to mitigate CdS photocorrosion for robust hydrogen production. *Chem. Eng. Sci.* **2026**, *331*, 123996. [CrossRef]
127. Li, D.; Zheng, W.; Gali, S.M.; Sobczak, K.; Horák, M.; Polčák, J.; Lopatik, N.; Li, Z.; Zhang, J.; Sabaghi, D.; et al. MXenes with ordered triatomic-layer borate polyanion terminations. *Nat. Mater.* **2024**, *23*, 1085–1092. [CrossRef] [PubMed]
128. Sun, W.; Shah, S.A.; Chen, Y.; Tan, Z.; Gao, H.; Habib, T.; Radovic, M.; Green, M.J. Electrochemical etching of Ti_2AlC to Ti_2CT_x (MXene) in low-concentration hydrochloric acid solution. *J. Mater. Chem. A* **2017**, *5*, 21663–21668. [CrossRef]
129. Lu, J.; Persson, I.; Lind, H.; Palisaitis, J.; Li, M.; Li, Y.; Chen, K.; Zhou, J.; Du, S.; Chai, Z.; et al. $Ti_{(n+1)}C_n$ MXenes with fully saturated and thermally stable Cl terminations. *Nanoscale Adv.* **2019**, *1*, 3680–3685. [CrossRef] [PubMed]
130. Shen, M.; Jiang, W.; Liang, K.; Zhao, S.; Tang, R.; Zhang, L.; Wang, J.-Q. One-pot green process to synthesize MXene with controllable surface terminations using molten salts. *Angew. Chem. Int. Ed.* **2021**, *60*, 27013–27018. [CrossRef] [PubMed]
131. Björk, J.; Rosén, J. Functionalizing MXenes by tailoring surface terminations in different chemical environments. *Chem. Mater.* **2021**, *33*, 9108–9118. [CrossRef]
132. Wei, S.; Zhang, P.; Xu, W.; Chen, S.; Xia, Y.; Cao, Y.; Zhu, K.; Cui, Q.; Wen, W.; Wu, C.; et al. Operando exploring and modulating phase evolution chemistry from MAX to MXenes in molten salt synthesis. *J. Am. Chem. Soc.* **2023**, *145*, 10681–10690. [CrossRef] [PubMed]
133. Yue, F.; Xiang, M.; Zheng, J.; Zhu, J.; Wei, J.; Yang, P.; Shi, H.; Dong, Q.; Ding, W.; Chen, C.; et al. One-step gas-phase syntheses of few-layered single-phase Ti_2NCl_2 and Ti_2CCl_2 MXenes with high stabilities. *Nat. Commun.* **2024**, *15*, 10334. [CrossRef] [PubMed]

134. Persson, I.; Halim, J.; Lind, H.; Hansen, T.W.; Wagner, J.B.; Näslund, L.-Å.; Darakchieva, V.; Palisaitis, J.; Rosen, J.; Persson, P.O.Å. 2D transition metal carbides (MXenes) for carbon capture. *Adv. Mater.* **2019**, *31*, e1805472. [CrossRef] [PubMed]
135. Persson, I.; Näslund, L.-Å.; Halim, J.; Barsoum, M.W.; Darakchieva, V.; Palisaitis, J.; Rosen, J.; Persson, P.O.Å. On the organization and thermal behavior of functional groups on Ti_3C_2 MXene surfaces in vacuum. *2D Mater.* **2018**, *5*, 015002. [CrossRef]
136. Näslund, L.-Å.; Mikkelä, M.-H.; Kokkonen, E.; Magnuson, M. Chemical bonding of termination species in 2D carbides investigated through valence-band UPS/XPS of $Ti_3C_2T_x$ MXene. *2D Mater.* **2021**, *8*, 045026. [CrossRef]
137. Hope, M.A.; Forse, A.C.; Griffith, K.J.; Lukatskaya, M.R.; Ghidiu, M.; Gogotsi, Y.; Grey, C.P. NMR reveals the surface functionalisation of Ti_3C_2 MXene. *Phys. Chem. Chem. Phys.* **2016**, *18*, 5099–5102. [CrossRef] [PubMed]
138. Yoo, R.M.S.; Djire, A. Decoupling the surface and bulk reactivities of MXenes and catalytic activity tuning through surface chemistry modification. *ACS Catal.* **2023**, *13*, 6823–6836. [CrossRef]
139. Ontiveros, D.; Viñes, F.; Sousa, C. MXenes surface termination under photoexcitation: Insights from excited-state Pourbaix diagrams. *ACS Appl. Mater. Interfaces* **2026**, *18*, 16573–16582. [CrossRef] [PubMed]
140. Ding, H.; Tong, X.; Zhang, Y. Surface reduction boosts free electron concentration in MXene for enhanced photothermal performance. *Sci. Adv.* **2026**, *12*, eaee2009. [CrossRef] [PubMed]
141. Li, Y.; Ding, L.; Guo, Y.; Liang, Z.; Cui, H.; Tian, J. Boosting the photocatalytic ability of g-C_3N_4 for hydrogen production by Ti_3C_2 MXene quantum dots. *ACS Appl. Mater. Interfaces* **2019**, *11*, 41440–41447. [CrossRef] [PubMed]
142. Du, X.; Zhao, T.; Xiu, Z.; Xing, Z.; Li, Z.; Pan, K.; Yang, S.; Zhou, W. $BiVO_4$@$ZnIn_2S_4$/Ti_3C_2 MXene quantum dots assembly all-solid-state direct Z-scheme photocatalysts for efficient visible-light-driven overall water splitting. *Appl. Mater. Today* **2020**, *20*, 100719. [CrossRef]
143. Dong, G.; Zhang, Y.; Wang, Y.; Deng, Q.; Qin, C.; Hu, Y.; Zhou, Y.; Tian, G. Ti_3C_2 quantum dots modified 3D/2D TiO_2/g-C_3N_4 S-scheme heterostructures for highly efficient photocatalytic hydrogen evolution. *ACS Appl. Energy Mater.* **2021**, *4*, 14342–14351. [CrossRef]
144. Chang, B.; Guo, Y.; Liu, H.; Li, L.; Yang, B. Engineering a surface defect-rich Ti_3C_2 quantum dots/mesoporous C_3N_4 hollow nanosphere Schottky junction for efficient N_2 photofixation. *J. Mater. Chem. A* **2022**, *10*, 3134–3145. [CrossRef]
145. Wei, P.; Chen, Y.; Zhou, T.; Wang, Z.; Zhang, Y.; Wang, H.; Yu, H.; Jia, J.; Zhang, K.; Peng, C. Manipulation of charge-transfer kinetics via $Ti_3C_2T_x$ (T = −O) quantum dot and N-doped carbon dot coloading on CdS for photocatalytic hydrogen production. *ACS Catal.* **2023**, *13*, 587–600. [CrossRef]
146. Agresti, A.; Pescetelli, S.; Viskadouros, G.; Pazniak, A.; Leonardi, E.; Di Vito, A.; Amiri, P.; Auf Der Maur, M.; Menchini, F.; Del Gobbo, S.; et al. MXene-driven nanoscale field-effect junction for advanced 4-terminal perovskite/silicon tandem solar panels. *Nat. Commun.* **2026**, *17*, 3394. [CrossRef] [PubMed]
147. Huang, Y.; Wang, X.; Zhang, H.; Gao, L.; Meng, J.; Liao, Y.; Zhou, Q.; Wei, Y.; Zong, B.; Li, H.; et al. Nb2C MXene quantum dots modulate built-in electric field within heterostructures for efficient solar-to-H_2O_2 conversion from seawater. *Appl. Catal. B Environ. Energy* **2025**, *371*, 125262. [CrossRef]
148. Hamdan, S.W.; Yusuf, A.O.; Othman, I.; Al Jitan, S.; Helal, M.I.; Žerjav, G.; Pintar, A.; Vega, L.F.; Al-Ali, K.; Palmisano, G. Ti_3C_2 MXene quantum dots-modified 2D/3D Ni_2P/$Zn_{0.5}Cd_{0.5}S$ heterostructures for efficient solar-driven hydrogen evolution. *J. Environ. Chem. Eng.* **2026**, *14*, 121851. [CrossRef]
149. Wang, Y.; Li, X.; Sun, L.; Yuan, H.; Sun, X. Efficient piezo-photocatalytic production of hydrogen by Ti_3C_2 MXene quantum dots modified $BaTiO_3$ nanowires. *J. Photochem. Photobiol. A Chem.* **2026**, *470*, 116649. [CrossRef]
150. Han, M.; Maleski, K.; Shuck, C.E.; Yang, Y.; Glazar, J.T.; Foucher, A.C.; Hantanasirisakul, K.; Sarycheva, A.; Frey, N.C.; May, S.J.; et al. Tailoring electronic and optical properties of MXenes through forming solid solutions. *J. Am. Chem. Soc.* **2020**, *142*, 19110–19118. [CrossRef] [PubMed]
151. Yazdanparast, S.; Soltanmohammad, S.; Fash-White, A.; Tucker, G.J.; Brennecka, G.L. Synthesis and surface chemistry of 2D TiVC solid-solution MXenes. *ACS Appl. Mater. Interfaces* **2020**, *12*, 20129–20137. [CrossRef] [PubMed]
152. Pinto, D.; Anasori, B.; Avireddy, H.; Shuck, C.E.; Hantanasirisakul, K.; Deysher, G.; Morante, J.R.; Porzio, W.; Alshareef, H.N.; Gogotsi, Y. Synthesis and electrochemical properties of 2D molybdenum vanadium carbides-solid solution MXenes. *J. Mater. Chem. A* **2020**, *8*, 8957–8968. [CrossRef]
153. Wang, L.; Han, M.; Shuck, C.E.; Wang, X.; Gogotsi, Y. Adjustable electrochemical properties of solid-solution MXenes. *Nano Energy* **2021**, *88*, 106308. [CrossRef]
154. Du, Z.; Wu, C.; Chen, Y.; Cao, Z.; Hu, R.; Zhang, Y.; Gu, J.; Cui, Y.; Chen, H.; Shi, Y.; et al. High-entropy atomic layers of transition-metal carbides (MXenes). *Adv. Mater.* **2021**, *33*, 2101473. [CrossRef] [PubMed]
155. Zhou, J.; Tao, Q.; Ahmed, B.; Palisaitis, J.; Persson, I.; Halim, J.; Barsoum, M.W.; Persson, P.O.Å.; Rosen, J. High-entropy laminate metal carbide (MAX phase) and its two-dimensional derivative MXene. *Chem. Mater.* **2022**, *34*, 2098–2106. [CrossRef]
156. Ma, W.; Qiu, Z.; Wang, M.; Tan, C.; Hu, L.; Lv, X.; Li, Q.; Li, J.; Dang, J. A novel high-entropy MXene $Ti_{1.1}V_{1.2}Cr_{0.8}Nb_{1.0}Mo_{0.9}C_4T_x$ for high-performance supercapacitor. *Scr. Mater.* **2023**, *235*, 115596. [CrossRef]

157. Tan, C.; Ma, W.; Hu, L.; Li, Q.; Lv, X.; Dang, J. Fabrication of novel $Ti_{1.1}V_{1.1}Cr_{0.4}Nb_{1.4}C_3T_x$ medium-entropy MXene through the thermodynamic competition strategy. *Acta Mater.* **2024**, *267*, 119713. [CrossRef]
158. Wyatt, B.C.; Yang, Y.; Michałowski, P.P.; Parker, T.; Morency, Y.; Urban, F.; Kadagishvili, G.; Tanwar, M.; Muhoza, S.P.; Nemani, S.K.; et al. Order-to-disorder transition due to entropy in layered and 2D carbides. *Science* **2025**, *389*, 1054–1058. [CrossRef] [PubMed]
159. Liu, Y.; Chen, M. Multihyperuniformity in high-entropy MXenes. *Appl. Phys. Lett.* **2025**, *126*, 013101. [CrossRef]
160. Ghoncheh, M.H.; Chen, Z.W.; Demingos, P.G.; Singh, C.V. Hydrogen evolution reaction in high-entropy MXenes: Insights into atomic configurations. *iScience* **2025**, *28*, 113436. [CrossRef] [PubMed]
161. Ma, W.; Qiu, Z.; Li, J.; Hu, L.; Li, Q.; Lv, X.; Dang, J. Interfacial electronic coupling of V-doped Co_2P with high-entropy MXene reduces kinetic energy barrier for efficient overall water splitting. *J. Energy Chem.* **2023**, *85*, 301–309. [CrossRef]
162. Huang, Y.; Gu, H.; Zhang, H.; Wang, X.; Gao, L.; Cui, Y.; Zong, B.; Li, H.; Dai, W.-L. Synergistic V–Nb sites modulate selective alkene epoxidation with in situ photogenerated H_2O_2 over COF@MXene heterostructures. *ACS Catal.* **2024**, *14*, 12541–12550. [CrossRef]
163. Li, Y.-H.; Zhang, F.; Chen, Y.; Li, J.-Y.; Xu, Y.-J. Photoredox-catalyzed biomass intermediate conversion integrated with H_2 production over $Ti_3C_2T_x$/CdS composites. *Green Chem.* **2020**, *22*, 163–169. [CrossRef]
164. Li, J.-Y.; Li, Y.-H.; Zhang, F.; Tang, Z.-R.; Xu, Y.-J. Visible-light-driven integrated organic synthesis and hydrogen evolution over 1D/2D CdS-$Ti_3C_2T_x$ MXene composites. *Appl. Catal. B Environ.* **2020**, *269*, 118783. [CrossRef]
165. Cao, B.; Wan, S.; Wang, Y.; Guo, H.; Ou, M.; Zhong, Q. Highly-efficient visible-light-driven photocatalytic H_2 evolution integrated with microplastic degradation over MXene/$Zn_xCd_{1-x}S$ photocatalyst. *J. Colloid Interface Sci.* **2022**, *605*, 311–319. [CrossRef] [PubMed]
166. Yuan, H.; Yang, J.; Zhang, Y.-W. Atomic-level design principles for the hydrogen evolution reaction on high-entropy MXene catalysts. *Nanoscale* **2026**, *18*, 13916–13924. [CrossRef] [PubMed]
167. Wu, D.; Tong, Z.; Wang, J.; Chen, G.; Zhu, A.; Tong, H.; Dang, M. Hole transfer promotion on La-MOF@MXene by valence band structure regulation for the efficient photocatalytic degradation. *Sep. Purif. Technol.* **2025**, *359*, 130873. [CrossRef]
168. Cabrero-Antonino, M.; Uscategui-Linares, A.; Ramírez-Grau, R.; García-Aznar, P.; Sastre, G.; Zhang, J.; Goberna-Ferrón, S.; Albero, J.; Yu, J.; García, H.; et al. 2D/2D MOF/MXene Schottky junction: Prolonged carrier lifetime and enhanced hydrogen evolution efficiency. *Angew. Chem. Int. Ed.* **2025**, *64*, e202503860. [CrossRef] [PubMed]
169. Abraham, B.M.; Sinha, P.; Halder, P.; Singh, J.K. Fusing a machine learning strategy with density functional theory to hasten the discovery of 2D MXene-based catalysts for hydrogen generation. *J. Mater. Chem. A* **2023**, *11*, 8091–8100. [CrossRef]
170. Abraham, B.M.; Piqué, O.; Khan, M.A.; Viñes, F.; Illas, F.; Singh, J.K. Machine learning-driven discovery of key descriptors for CO_2 activation over two-dimensional transition metal carbides and nitrides. *ACS Appl. Mater. Interfaces* **2023**, *15*, 30117–30126. [CrossRef] [PubMed]
171. Shaw, S.; Ghosh, S. Computational study based prediction of new photocatalysts for water splitting by systematic manipulation of MXene surfaces. *J. Mater. Chem. C* **2024**, *12*, 9146–9157. [CrossRef]
172. Ontiveros, D.; Vela, S.; Viñes, F.; Sousa, C. MXgap: A MXene learning tool for bandgap prediction. *ACS Catal.* **2025**, *15*, 1440314413. [CrossRef] [PubMed]
173. Tang, K.; Liu, S.; Zhou, J.; Sun, Z. Deep-learning-enabled high-throughput screening of MXene photocatalysts for hydrogen production. *Nanoscale* **2025**, *17*, 21717–21728. [CrossRef] [PubMed]
174. Nassar, K.I.; Galvão, T.L.P.; Gouveia, J.D.; Gomes, J.R.B. Predicting adsorption energies on MXene surfaces using machine learning to enhance catalyst design for the water–gas shift reaction. *J. Phys. Chem. C* **2025**, *129*, 2512–2524. [CrossRef]
175. Habib, T.; Zhao, X.; Shah, S.A.; Chen, Y.; Sun, W.; An, H.; Lutkenhaus, J.L.; Radovic, M.; Green, M.J. Oxidation stability of $Ti_3C_2T_x$ MXene nanosheets in solvents and composite films. *npj 2D Mater. Appl.* **2019**, *3*, 8. [CrossRef]
176. Doo, S.; Chae, A.; Kim, D.; Oh, T.; Ko, T.Y.; Kim, S.J.; Koh, D.-Y.; Koo, C.M. Mechanism and kinetics of oxidation reaction of aqueous $Ti_3C_2T_x$ suspensions at different pHs and temperatures. *ACS Appl. Mater. Interfaces* **2021**, *13*, 22855–22865. [CrossRef] [PubMed]
177. Wu, T.; Kent, P.R.C.; Gogotsi, Y.; Jiang, D.-E. How water attacks MXene. *Chem. Mater.* **2022**, *34*, 4975–4982. [CrossRef]
178. Xu, W.; Yu, Z.; Yang, H.; An, X.; Peng, C.; Yang, G.; Wang, H.-F.; Cao, Y.; Wang, H.; Yu, H. Engineering charge transfer of MXene-hybridized photocatalysts: An in situ Kelvin probe atomic force microscopy study. *Small* **2026**, *22*, e13542. [CrossRef] [PubMed]
179. Dessoliers, Z.; Chemin, A.; Valurouthu, G.; Lord, R.; Bilyk, T.; Gogotsi, Y.; Mauchamp, V.; Petit, T. Combining X-ray photoelectron and absorption spectroscopies for determining surface chemistry and composition of $Ti_3C_2T_x$ MXene. *Adv. Mater. Interfaces* **2025**, *12*, 2500391. [CrossRef]
180. Xin, H.; Kitchin, J.R.; López, N.; Schweitzer, N.M.; Artrith, N.; Che, F.; Grabow, L.C.; Gunasooriya, G.T.K.K.; Kulik, H.J.; Laino, T.; et al. Roadmap for transforming heterogeneous catalysis with artificial intelligence. *Nat. Catal.* **2026**, *9*, 102–111. [CrossRef]

181. Burger, B.; Maffettone, P.M.; Gusev, V.V.; Aitchison, C.M.; Bai, Y.; Wang, X.; Li, X.; Alston, B.M.; Li, B.; Clowes, R.; et al. A mobile robotic chemist. *Nature* **2020**, *583*, 237–241. [CrossRef] [PubMed]
182. Yang, H.; Che, Y.; Cooper, A.I.; Chen, L.; Li, X. Machine learning accelerated exploration of ternary organic heterojunction photocatalysts for sacrificial hydrogen evolution. *J. Am. Chem. Soc.* **2023**, *145*, 27038–27044. [CrossRef] [PubMed]
183. Timoshenko, J.; Haase, F.T.; Saddeler, S.; Rüscher, M.; Jeon, H.S.; Herzog, A.; Hejral, U.; Bergmann, A.; Schulz, S.; Roldan Cuenya, B. Deciphering the structural and chemical transformations of oxide catalysts during oxygen evolution reaction using quick X-ray absorption spectroscopy and machine learning. *J. Am. Chem. Soc.* **2023**, *145*, 4065–4080. [CrossRef] [PubMed]
184. Szymanski, N.J.; Rendy, B.; Fei, Y.; Kumar, R.E.; He, T.; Milsted, D.; McDermott, M.J.; Gallant, M.; Cubuk, E.D.; Merchant, A.; et al. An autonomous laboratory for the accelerated synthesis of inorganic materials. *Nature* **2023**, *624*, 86–91. [CrossRef] [PubMed]
185. Moon, J.; Beker, W.; Siek, M.; Kim, J.; Lee, H.S.; Hyeon, T.; Grzybowski, B.A. Active learning guides discovery of a champion four-metal perovskite oxide for oxygen evolution electrocatalysis. *Nat. Mater.* **2024**, *23*, 108–115. [CrossRef] [PubMed]
186. Zhang, W.; Yu, M.; Liu, T.; Cong, M.; Liu, X.; Yang, H.; Bai, Y.; Zhu, Q.; Zhang, S.; Gu, H.; et al. Accelerated discovery of molecular nanojunction photocatalysts for hydrogen evolution by using automated screening and flow synthesis. *Nat. Synth.* **2024**, *3*, 595–605. [CrossRef]

Disclaimer/Publisher's Note: The statements, opinions and data contained in all publications are solely those of the individual author(s) and contributor(s) and not of MDPI and/or the editor(s). MDPI and/or the editor(s) disclaim responsibility for any injury to people or property resulting from any ideas, methods, instructions or products referred to in the content.